The Astronomical Journal, 145:138 (28pp), 2013 May doi:10.1088/0004-6256/145/5/138

THE VIRUS-P EXPLORATION OF NEARBY GALAXIES (VENGA): SURVEY DESIGN, DATA PROCESSING, AND SPECTRAL ANALYSIS METHODS

Guillermo A. Blanc[1], Tim Weinzirl[2], Mimi Song[2], Amanda Heiderman[2], Karl Gebhardt[2], Shardha Jogee[2], Neal J. Evans II[2], Remco C. E. van den Bosch[3], Rongxin Luo[4], Niv Drory[5], Maximilian Fabricius[6], David Fisher[7], Lei Hao[4], Kyle Kaplan[2], Irina Marinova[2], Nalin Vutisalchavakul[2], and Peter Yoachim[8]
[1] Observatories of the Carnegie Institution for Science, Pasadena, CA, USA
[2] Department of Astronomy, The University of Texas at Austin, Austin, TX, USA
[3] Max Planck Institute for Astronomy, Heidelberg, Germany
[4] Shanghai Astronomical Observatory, Shanghai, China
[5] Instituto de Astronomía, Universidad Nacional Autónoma de México, México, DF, Mexico
[6] Max Planck Institute for Extraterrestrial Physics, Garching, Germany
[7] Department of Astronomy, University of Maryland, College Park, MD, USA
[8] Astronomy Department, University of Washington, Seattle, WA, USA
Received 2012 August 27; accepted 2013 February 27; published 2013 April 9

ABSTRACT

We present the survey design, data reduction, and spectral fitting pipeline for the VIRUS-P Exploration of Nearby Galaxies (VENGA). VENGA is an integral field spectroscopic survey, which maps the disks of 30 nearby spiral galaxies. Targets span a wide range in Hubble type, star formation activity, morphology, and inclination. The VENGA data cubes have 5.″6 FWHM spatial resolution, ∼5 Å FWHM spectral resolution, sample the 3600 Å–6800 Å range, and cover large areas typically sampling galaxies out to $\sim 0.7 R_{25}$. These data cubes can be used to produce two-dimensional maps of the star formation rate, dust extinction, electron density, stellar population parameters, the kinematics and chemical abundances of both stars and ionized gas, and other physical quantities derived from the fitting of the stellar spectrum and the measurement of nebular emission lines. To exemplify our methods and the quality of the data, we present the VENGA data cube on the face-on Sc galaxy NGC 628 (a.k.a. M 74). The VENGA observations of NGC 628 are described, as well as the construction of the data cube, our spectral fitting method, and the fitting of the stellar and ionized gas velocity fields. We also propose a new method to measure the inclination of nearly face-on systems based on the matching of the stellar and gas rotation curves using asymmetric drift corrections. VENGA will measure relevant physical parameters across different environments within these galaxies, allowing a series of studies on star formation, structure assembly, stellar populations, chemical evolution, galactic feedback, nuclear activity, and the properties of the interstellar medium in massive disk galaxies.

Key words: galaxies: general – galaxies: kinematics and dynamics – galaxies: spiral – ISM: kinematics and dynamics – methods: data analysis – surveys

Online-only material: color figures

1. INTRODUCTION

In the context of ΛCDM cosmology, the formation and evolution of galaxies takes place in the bottom of the deepest gravitational potential wells in the dark matter distribution (dark matter halos). Gas accretion into these halos and merging processes ultimately trigger star formation, giving rise to galaxies (Blumenthal et al. 1984; White et al. 1988; Somerville & Primack 1999). Although a consensus has been reached concerning this picture, the details of the baryonic physics behind galaxy formation in the centers of dark matter halos are still aggressively debated. The triggering of star formation and the variables that set the star formation rate (SFR; Kennicutt 1998; Kennicutt & Evans 2012; McKee & Ostriker 2007; Leroy et al. 2008; Krumholz et al. 2009), the contribution from different types of feedback processes (active galactic nuclei, supernovae, stellar radiation, e.g., Kauffmann et al. 1999; Croton et al. 2006; Thompson 2009), as well as the impact of gas accretion from the intergalactic medium (e.g., Dekel et al. 2009; Fumagalli et al. 2011; Davé et al. 2011; van de Voort et al. 2012), at regulating the gaseous budget, structure, chemical composition, and kinematics of the interstellar medium (ISM), and the role that major and minor mergers as well as secular evolution processes play in shaping galaxies (Toomre & Toomre 1972; Kormendy & Kennicutt 2004), are currently the subjects of active research. All these processes play a major role in determining how galaxies evolve throughout cosmic time, building up their stellar mass and shaping their present-day structure.

The detailed manner in which the above physical phenomena (star formation, gas accretion, feedback, interactions, and secular evolution) proceed ultimately determines the morphology, kinematics, and chemical structure of both the ISM and stellar components of a galaxy. We can therefore study these processes by obtaining spatially resolved measurements of quantities like the SFR, the metallicity, the stellar and ionized gas velocity and velocity dispersion, the age of the observed stellar populations, the atomic and molecular gas surface density, etc., and by analyzing how they relate to each other and to the global properties of the galaxies under study. In this way, we can test current theoretical models describing the above phenomena and their impact on galaxy evolution.

Wide-field optical integral field unit (IFU) spectroscopy allows the measurement of many of these quantities in nearby galaxies. Optical IFU data cubes, in combination with multi-wavelength broadband photometry, and sub-mm and radio maps of the same galaxies, are powerful data sets with which to study galaxy evolution.

Integral field spectroscopy of nearby galaxies has been somewhat limited in the past, mostly due to the small field of view (FOV) of available IFUs. During the last decade, a

new generation of wide-field integral field spectrographs like SAURON on the 4.2 m William Herschel Telescope (Bacon et al. 2001), PPAK on the 3.5 m at Calar Alto Observatory (Kelz et al. 2006), SparsePak on the WIYN 3.5 m telescope (Bershady et al. 2004), and the Mitchell Spectrograph (formerly known and hereafter referred to as VIRUS-P) on the 2.7 m Harlan J. Smith telescope at McDonald Observatory (Hill et al. 2008) have opened the path to study nearby systems subtending large angular diameters on the sky.

Early surveys of nearby galaxies using IFUs mostly focused on studying the kinematics and stellar populations of early-type systems. These include the SAURON Survey (Bacon et al. 2001; de Zeeuw et al. 2002) and its extension, the Atlas3D Survey (Cappellari et al. 2011), which by now have mapped hundreds of elliptical and lenticular galaxies. Wide-field IFU studies of later-type disk galaxies include the work of Ganda et al. (2006) who used SAURON to observe the central regions of 18 nearby late-type spirals, the Disk Mass Project (Bershady et al. 2010a), which used SparsePak and PPAK to measure Hα velocity fields for 146 face-on spirals, and stellar kinematics for a subset of 46 objects, with the aim of constraining the distribution of stellar mass and dark matter in disk galaxies, and the PPAK IFS Nearby Galaxies Survey (PINGS; Rosales-Ortega et al. 2010), which maps the disks of 17 nearby disk galaxies. The PPAK IFU is currently being used to conduct the Calar Alto Legacy Integral Field Area survey (CALIFA; Sanchez et al. 2012), a massive project mapping ~600 galaxies of all Hubble types, selected based on their angular size and distance (in order for them to fill the PPAK FOV). In the future, the MANGA SDSS IV project[9] will produce optical data cubes for tens of thousands of galaxies. A number of IFU studies of galaxies have been conducted at high redshift ($1 < z < 3$), where target sizes are well suited to the small FOVs of IFUs in 10 m class telescopes (e.g., Genzel et al. 2006; Förster Schreiber et al. 2006; Law et al. 2007; Wright et al. 2007; Lemoine-Busserolle et al. 2010).

In this work, we present the VIRUS-P Exploration of Nearby Galaxies (VENGA), an IFU survey of 30 nearby spirals that uses VIRUS-P (currently the IFU with the largest FOV in the world) to spectroscopically map large portions of the disks of these objects. The sample spans a wide range in Hubble types, SFRs, and morphologies, including galaxies with classical and pseudo-bulges as well as barred and unbarred objects. Ancillary multi-wavelength data exist for many of the targets. This includes *Hubble Space Telescope* optical and near-IR imaging with ACS and NICMOS, *Spitzer* mid-IR and far-IR imaging with IRAC and MIPS, near-UV and far-UV imaging from *GALEX*, and far-IR *Herschel* data. Also, CO and H I 21 cm maps are available for most of the sample. VENGA's potential lies in a combination of wide spatial and spectral coverage, good spatial resolution, and depth. The large $1.'7 \times 1.'7$ FOV of the IFU allows us to typically sample each system out to $\sim 0.7 R_{25}$ by tiling only a few VIRUS-P pointings. The size of the VIRUS-P optical fibers ($4.''24$ in diameter) samples physical scales of ~300 pc at the median distance of our targets and makes our observations very sensitive to low-surface brightness emission. We obtain spectra with a median signal-to-noise ratio (S/N) = 40 per fiber per spectral resolution element, which allows good measurements of stellar absorption and nebular emission line spectral features at the native spatial resolution of the instrument over most of the data cube for every galaxy.

[9] http://www.sdss3.org/future/

In comparison to other IFU surveys of spiral galaxies, VENGA is a factor of a few deeper than surveys like PINGS and CALIFA while having a similar wavelength coverage and a factor of two larger spatial resolution. As mentioned above a key advantage of the VENGA sample is the existence of extensive multi-wavelength ancillary data for most of these very nearby galaxies. In particular the far-IR, mm, and radio data are essential for studying the relation between stars and the ISM and the process of star formation. While CALIFA and in the future MANGA will produce data cubes for hundreds and tens of thousands of spiral galaxies, only a few of those targets will have such extensive ancillary data sets. In that sense the VENGA data can provide a good base for interpreting the results from larger but shallower surveys of more distant galaxies.

In the near future, VENGA will also include a high spectral resolution component consisting of IFU mapping at $R \sim 6000$ of the central regions of a subset of the sample using the VIRUS-W spectrograph (Fabricius et al. 2008). The high-resolution VIRUS-W observations will complement the broad wavelength range VIRUS-P observations and will provide a more detailed view of the kinematics of gas and stars in the central regions of spiral galaxies. This component of the survey will be presented in a future publication. In this work we limit ourselves to discussing the VIRUS-P data.

The VENGA data are being used to conduct an extensive set of studies on star formation, structure assembly, stellar populations, gas and stellar dynamics, chemical evolution, ISM structure, and galactic feedback. The data will also provide an excellent local universe control sample for IFU studies of high-z galaxies. The survey is designed with the following science goals:

1. Study the process of star formation on galactic scales (Kennicutt & Evans 2012 and references therein), including the correlations between the SFR and the star formation efficiency (SFE) with other parameters like gas and stellar surface density, metallicity, galaxy dynamics, and stellar populations. The ultimate goal is to understand what are the relevant parameters setting the SFR across different environments within galaxies (see Blanc et al. 2009, 2013).
2. Investigate the assembly of central spheroidal stellar components in disk galaxies (Kormendy & Kennicutt 2004 and references therein). This includes characterizing the dynamics, stellar populations, and chemical abundances of classical and pseudo-bulges in spiral galaxies, in order to constrain their star formation history and understand their origin. The goal is to distinguish between different evolutionary paths that might give rise to these structures (secular evolution, galaxy–galaxy interactions, etc.).
3. Provide detailed observations of radial gas inflow in the central parts of disk galaxies, induced by barred and oval potentials (Kormendy & Kennicutt 2004 and references therein). This includes studying the velocity field of ionized gas and stars in the regions influenced by the presence of bars and ovals, and also the effects of induced gas condensation and shocks in the local SFE.
4. Construct two-dimensional maps of the stellar and gas phase metallicity of spiral galaxies (e.g., Moustakas et al. 2010; Rosales-Ortega et al. 2011). These maps will allow the study of radial abundance gradients measured with exquisite detail, the dispersion in abundances as a function of galactocentric radius, and deviations from axisymmetry in the two-dimensional metallicity distribution. Comparing

these measurements to chemical evolution models will help constrain the chemical enrichment, gas accretion, and star formation history of disk galaxies in the local universe.

5. Use nebular emission line diagnostics to study the nature of the ionizing sources influencing different parts of the disks of spirals (e.g., Kewley et al. 2001; Ho 2008; Haffner et al. 2009 and references therein). This includes the study of low-luminosity active galactic nuclei, and their impact on the physical conditions of gas in the central parts of galaxies, and the study of the structure, metallicity, and kinematics of the diffuse ionized gas (DIG) in the ISM. In particular, for the two edge-on systems in the sample, we will also be able to constrain the properties of the DIG as a function of distance above the midplane. All these studies will provide insight about different feedback processes at play in star-forming disk galaxies, and the transport of UV photons in the multi-phase ISM.
6. Study the distribution of stellar mass and dark matter in spiral galaxies, by using a combination of the VENGA gas and stellar velocity fields and constraints on the M/L ratio from stellar populations (e.g., Bershady et al. 2010a; Adams et al. 2012). The data should allow us, in principle, to set constraints on the shape of the dark matter halo density profile on these systems, which we can use to test the predictions of ΛCDM models. Of particular importance for these measurements is the high spectral resolution VIRUS-W component of the survey.

Throughout this paper we use the VENGA data on the face-on SA(s)c galaxy NGC 628 to exemplify our methodology. This nearby grand-design spiral galaxy has been extensively studied in the past and IFU spectroscopy has been obtained in its central region by Ganda et al. (2006) and over a larger area than presented here, although to a shallower depth, by the PINGS survey (Rosales-Ortega et al. 2011; Sanchez et al. 2011). In this work we limit ourselves to presenting the methods used to observe, reduce, and analyze the VENGA IFU data, and we postpone the presentation of scientific results on NGC 628 to separate publications, including an accompanying paper studying the radial profile of the CO to H_2 conversion factor (X_{CO}) and its relation to the physical conditions across the disk of the galaxy (Blanc et al. 2013). We also expect to present and make public the full VENGA data set in a future publication once the processing and analysis of the whole survey is complete.

In Section 2 we describe the survey design, including a description of the VENGA sample and the observing strategy adopted to conduct the survey. We present the VIRUS-P observations of NGC 628 in Section 3. The data processing pipeline and construction of the final VENGA data products (i.e., reduced and calibrated spectral data cubes) are presented in Section 4, followed by a description of the techniques used to fit the spectra, measure stellar and gas kinematics, and extract emission line fluxes (Section 5). In Section 6 we fit the stellar and ionized gas velocity fields of NGC 628 using a harmonic decomposition technique and introduce a new method to measure the inclination of nearly face-on systems based on the matching of the stellar and gas rotation curves using asymmetric drift corrections. Finally, we present our conclusions in Section 7. Throughout the paper we adopt a standard set of ΛCDM cosmological parameters, $H_o = 70$ km s^{-1}Mpc^{-1}, $\Omega_M = 0.3$, and $\Omega_\Lambda = 0.7$ (Dunkley et al. 2009).

2. SURVEY DESIGN

In this section we present and characterize the VENGA sample and we discuss the physical properties of the target galaxies. We also describe the observing strategy and the instrumental configurations used to execute the survey.

2.1. The VENGA Sample

Table 1 presents the galaxies observed in VENGA and lists their main properties. Targets are chosen to span a wide range in Hubble types, from S0 to Sd, a wide range in inclinations from face-on to edge-on systems, and they include both barred and unbarred objects. The sample also spans a wide range in right ascension in order to allow observations to be carried out throughout the whole year, and all objects have declinations $\delta > -10^\circ$ to make them accessible from McDonald Observatory. Figure 1 presents Digitized Sky Survey (DSS[10]) cutouts for all the galaxies in VENGA. Overlaid are the $1\farcm7 \times 1\farcm7$ VIRUS-P pointings obtained on each galaxy. While VENGA is designed to map galaxies out to $\sim 0.7 R_{25}$, for NGC 3198, NGC 4569, NGC 4826, NGC 5055, and NGC 7731, only a central pointing was observed due to observing time constraints.

Since one of the goals of VENGA is to study the origin and properties of stellar spheroids in the inner parts of disk galaxies, we include objects showing both classical bulges and pseudo-bulges (Kormendy & Kennicutt 2004 and references therein). To distinguish between these two types of stellar structures we adopt a criterion based on the Sérsic index of the spheroidal component (n_B). Following the results of Fisher & Drory (2008) we adopt a limit of $n_B = 2$. We consider classical bulges those with $n_B > 2$ and pseudo-bulges those with $n_B < 2$. Table 2 presents the bulge-to-total light fractions (B/T) and n_B values for 18 of the 30 VENGA galaxies taken from Dong & De Robertis (2006), Fisher & Drory (2008), and Weinzirl et al. (2009). Of the galaxies for which we found bulge Sérsic index measurements in the literature, 50% are classified as classical bulges and 50% as pseudo-bulges using the $n_B = 2$ criterion.

In order to understand how well the galaxies in our sample represent the overall population of galaxies in the local universe, we compare their stellar mass (M_*) and SFR distributions to that of $\sim 8 \times 10^5$ galaxies at $z < 0.2$ from the Sloan Digital Sky Survey (SDSS; York et al. 2000) MPA/JHU DR7[11] catalog of SFRs (Brinchmann et al. 2004). For the VENGA galaxies, we estimate M_* from their K-band luminosity by assuming a mass-to-light ratio of $\Upsilon_K = 0.78$ (de Jong 1996). The K-band luminosities are computed using the distances reported in Table 1 and the total K-band apparent magnitudes from the Two Micron All Sky Survey (2MASS) Large Galaxy Atlas (LGA; Jarrett et al. 2003) except for NGC 1042, NGC 3147, NGC 3949, NGC 5981, NGC 7479, and NGC 7331, which are not included in the LGA so their magnitudes are taken from the 2MASS Extended Source Catalog (Jarrett et al. 2000). We do not correct the luminosity for dust extinction but we expect this effect to be small ($\sim$10% in the K band).

We were able to find integrated SFR measurements in the literature for 24 of the 30 galaxies in the VENGA sample. These are taken from Lee et al. (2009), Kennicutt et al. (2003), and

[10] The Digitized Sky Surveys were produced at the Space Telescope Science Institute under U.S. Government grant NAG W-2166. The images of these surveys are based on photographic data obtained using the Oschin Schmidt Telescope on Palomar Mountain and the UK Schmidt Telescope. The plates were processed into the present compressed digital form with the permission of these institutions.

[11] http://www.mpa-garching.mpg.de/SDSS/

Table 1
The VENGA Sample

Object	Equatorial Coord.[a]		Type[a]	i[a]	θ[a]	d_{25}[a]	D	Method[b]	pc/"	M_K[c]	μ_B[a]	N_P
	α	δ		(deg)	(deg)	(arcmin)	(Mpc)			(mag)	(mag arcsec^{-2})	
NGC 337	00:59:50.0	−07:34:41	SB(s)d	52	130	2.9×1.8	19.5 ± 1.5	TF	95	-22.35 ± 0.18	21.54	1
NGC 628	01:36:41.7	15:47:00	SA(s)c	8.7[d]	21[d]	10.5×9.5	8.6 ± 0.3	PNLF	42	-22.83 ± 0.09	22.56	3
NGC 1042	02:40:24.0	−08:26:02	SAB(rs)cd	40	6[e]	4.7×3.6	4.2 ± 0.7	TF	20	-19.27 ± 0.36	23.27	2
NGC 1068	02:42:40.2	−00:00:48	SA(rs)b	32	70	7.1×6.0	10.1 ± 1.7	TF	49	-24.23 ± 0.36	19.54	3
NGC 2775	09:10:20.1	07:02:17	SA(r)ab	40	155	4.3×3.3	21.5 ± 1.5	Flow	104	-24.60 ± 0.15	20.94	3
NGC 2841	09:22:01.8	50:58:31	SA(r)b	67	147	8.1×3.5	14.1 ± 1.5	Ceph	68	-24.69 ± 0.23	21.43	3
NGC 2903	09:32:09.7	21:30:02	SB(s)d	64	17	12.6×6.0	8.6 ± 1.4	TF	41	-23.62 ± 0.35	21.31	3
NGC 3147	10:16:53.2	73:24:04	SA(rs)bc	28	155	3.9×3.5	43.1 ± 3.0	Flow	209	-25.76 ± 0.15	21.16	2
NGC 3166	10:13:45.0	03:25:31	SAB(rs)0	63	87	4.8×2.3	22.0 ± 1.5	Flow	107	-24.50 ± 0.15	20.38	2
NGC 3198	10:19:54.9	45:33:09	SB(rs)c	70	35	8.5×3.3	13.7 ± 0.5	Ceph	66	-22.90 ± 0.09	22.70	1
NGC 3227	10:23:31.5	19:51:48	SAB(s)pec	49	155	5.4×3.6	20.3 ± 1.4	Flow	99	-23.90 ± 0.15	22.60	2
NGC 3351	10:43:58.1	11:42:15	SB(r)b	49	13	7.4×5.0	9.6 ± 0.2	TRGB	47	-21.97 ± 0.05	21.57	2
NGC 3521	11:05:49.0	−00:02:15	SAB(rs)bc	64	163	11.0×5.1	11.2 ± 1.8	TF	54	-24.47 ± 0.35	20.69	3
NGC 3627	11:20:15.0	12:59:29	SAB(s)b	65	173	9.1×4.2	8.3 ± 0.3	TRGB	40	-23.71 ± 0.09	20.84	3
NGC 3938	11:52:49.8	44:07:26	SA(s)c	25	52[e]	5.4×4.9	15.6 ± 1.1	Flow	75	-23.15 ± 0.16	22.11	2
NGC 3949	11:53:41.5	47:51:35	SA(s)bc	57	120	2.9×1.7	19.1 ± 3.1	TF	92	-22.80 ± 0.35	...	1
NGC 4013	11:58:31.7	43:56:48	SAb	90	66	5.2×1.0	18.9 ± 3.1	TF	92	-23.75 ± 0.35	22.95	2
NGC 4254	12:18:49.4	14:25:07	SA(s)c	30	60[e]	5.4×4.7	14.3 ± 3.5	TF	70	-26.07 ± 0.15	21.16	3
NCG 4314	12:22:32.2	29:53:47	SB(rs)a	28	145[e]	4.2×3.7	9.7 ± 3.6	TF	87	-23.81 ± 0.15	21.11	2
NGC 4450	12:28:29.4	17:05:05	SA(s)ab	43	175	5.2×3.9	15.3 ± 2.5	TF	74	-23.87 ± 0.35	21.79	2
NGC 4569	12:36:50.1	13:09:48	SAB(rs)ab	65	23	9.5×4.4	9.9 ± 0.2	STF	48	-23.39 ± 0.06	22.10	1
NGC 4826	12:56:44.3	21:41:05	SA(rs)ab	59	115	10.0×5.4	4.4 ± 0.1	TRGB	21	-22.87 ± 0.03	20.69	1
NGC 5055	13:15:49.3	42:02:06	SA(rs)bc	57	105	12.6×7.2	9.0 ± 0.1	TRGB	44	-24.16 ± 0.03	21.39	1
NGC 5194	13:29:53.4	47:11:48	SA(s)bc	20[f]	163	11.2×6.9	9.1 ± 0.6	Flow	44	-24.30 ± 0.15	21.40	3
NGC 5713	14:40:11.6	−00:17:26	SAB(rs)bc	28	10	2.8×2.5	31.3 ± 2.2	Flow	152	-24.15 ± 0.15	21.36	1
NGC 5981	15:37:53.4	59:23:34	Sc	90	140	2.8×0.5	49.7 ± 9.2	TF	241	-24.19 ± 0.40	...	1
NGC 6503	17:49:27.7	70:08:41	SA(s)cd	74	123	7.1×2.4	4.0 ± 0.1	TRGB	19	-20.71 ± 0.04	21.08	2
NGC 6946	20:34:52.3	60:09:14	SAB(rs)cd	32	60[e]	11.5×9.8	6.1 ± 0.6	PNLF	29	-23.55 ± 0.21	22.93	2
NGC 7479	23:04:57.1	12:19:18	SB(s)c	42	25	4.1×3.1	30.2 ± 5.6	TF	146	-24.20 ± 0.40	22.42	2
NGC 7331	22:37:04.0	34:24:56	SA(s)b	72	171	10.5×3.7	14.5 ± 0.6	Ceph	70	-24.78 ± 0.09	21.51	1

Notes.
[a] Coordinates, inclination (i), position angle (θ), isophotal diameter (d_{25}), and effective B-band surface brightness (μ_B) taken from RC3 (de Vaucouleurs et al. 1991) except when indicated.
[b] Distance (D) methods and references; TRGB: Tip of the red giant branch (Jacobs et al. 2009; Tully et al. 2009) except for NGC 3351 taken from Rizzi et al. (2007); Ceph: Cepheid variables (Freedman et al. 2001, except for NGC 2841 taken from Macri et al. 2001); TF: H I 21 cm Tully–Fisher (Tully et al. 2009, for NGC 0337 we used the group Tully–Fisher distance) except for NGC 4252 taken from Springob et al. (2009); STF: Stellar kinematics Tully–Fisher (Cortés et al. 2008); PNLF: Planetary nebulae luminosity function (Herrmann et al. 2008); Flow: Derived from redshift, and corrected for peculiar velocities (Mould et al. 2000, taken from NED).
[c] From Jarrett et al. (2003) except for NGC 1042, NGC 3147, NGC 3949, NGC 5981, NGC 7479, and NGC 7331 taken from Jarrett et al. (2000).
[d] From this work.
[e] From Paturel et al. (2000) (NGC 1042, NGC 3938), Springob et al. (2009) (NGC 4254, NGC 6946), and Jarrett et al. (2003) (NGC 4314).
[f] For NGC 5194 we use kinematic inclination angle derived by Tully (1974).

Thilker et al. (2007) in that order of preference when multiple measurements are found. The stellar masses and SFRs of the VENGA galaxies are reported in Table 3. Figure 2 shows the VENGA and SDSS galaxies on the M_* versus SFR plane. Our sample spans a range in SFR from 0.2 to 39 $M_\odot$ yr^{-1} and is distributed in this parameter similarly to the star-forming SDSS galaxies. In term of stellar mass, the VENGA galaxies span a range between $8 \times 10^8\ M_\odot$ and $3 \times 10^{11} M_\odot$, but with 93% (28/30) of the sample having $M_* > 10^{10}\ M_\odot$. By comparing the stellar mass distribution to that of the SDSS star-forming galaxies it is evident that our sample is biased toward the high-mass end of the local star-forming population. Figure 2 shows that our targets fall both on and below the M_* − SFR main sequence of star-forming galaxies, so starburst systems are not present in the sample. The VIRUS-P Investigation of the Extreme Environments of Starbursts (VIXENS) project is conducting a similar study to VENGA but on a sample of 15 interacting/starburst galaxies in the local universe (Heiderman 2012). VENGA is primarily a survey of massive spiral galaxies. Dwarf galaxies, early-type galaxies, and starbursts are not well represented in the sample.

Finally, it is important to characterize the spatial resolution we can achieve with VIRUS-P at the distances of our targets. Table 1 reports the physical scale in parsecs corresponding to 1″ at the distance of each galaxy. The IFU fibers subtend a 4.″24 diameter on the sky, which corresponds to a spatial resolution between 80 pc for the closest galaxy (NGC 6503) and 1020 pc for the farthest (NGC 5981). As will be described in Section 4.7 the point-spread function (PSF) of the final data cubes is given by the convolution of the native instrumental resolution (set by the fiber size) with the seeing and a Gaussian weighting filter used to combine different frames at different dither positions. This translates into an effective PSF FWHM of 5.″6 in the final VENGA data cubes, which corresponds to a range in spatial resolution of 109 pc–1.35 kpc, and a median resolution of 383 pc. Figure 3 presents a histogram of the physical scale in parsecs of the VIRUS-P native fiber size (black) and the final data cube PSF FWHM (red) for our targets.

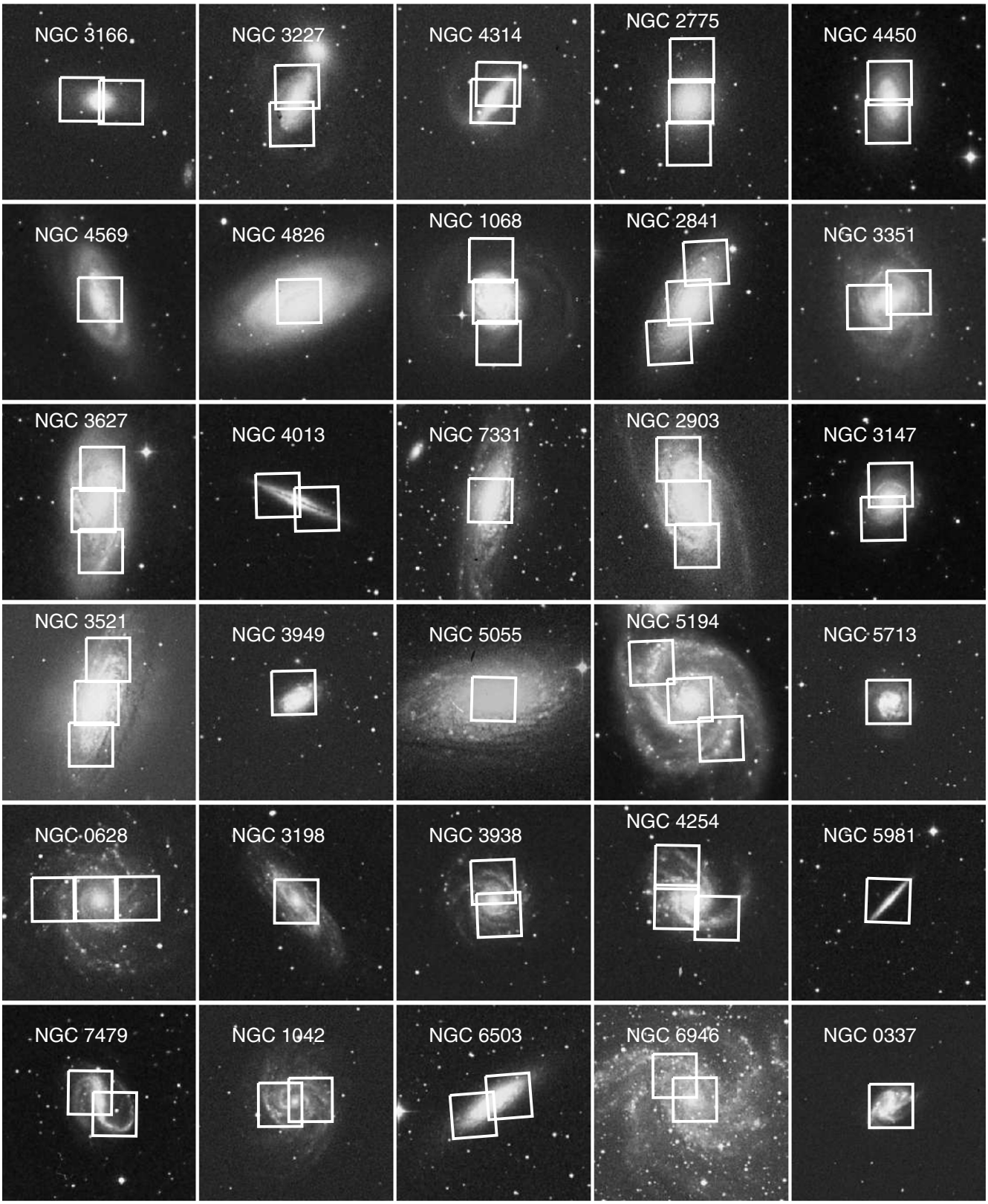

Figure 1. Digital Sky Survey cutouts of the 30 galaxies in the VENGA sample. The targets are ordered by Hubble type (taken from RC3; de Vaucouleurs et al. 1991) from earlier to later. White boxes show the VIRUS-P 1.′7 × 1.′7 pointings observed on each galaxy.

2.2. Observing Strategy

The VIRUS-P IFU is a square array of 246 optical fibers (each 4.″24 in diameter) that samples a 1.′7 × 1.′7 FOV with a 1/3 filling factor. Three dithers provide full coverage of the FOV. The instrument images the spectra of the 246 fibers on a 2k×2k Fairchild Instruments charged-coupled device (CCD) with 15 μm pixels. The CCD electronics deliver 3.6–4.3 e^- read noise depending on the readout mode used. Fiber spectra have an approximately Gaussian spatial profile of ∼5 pixels

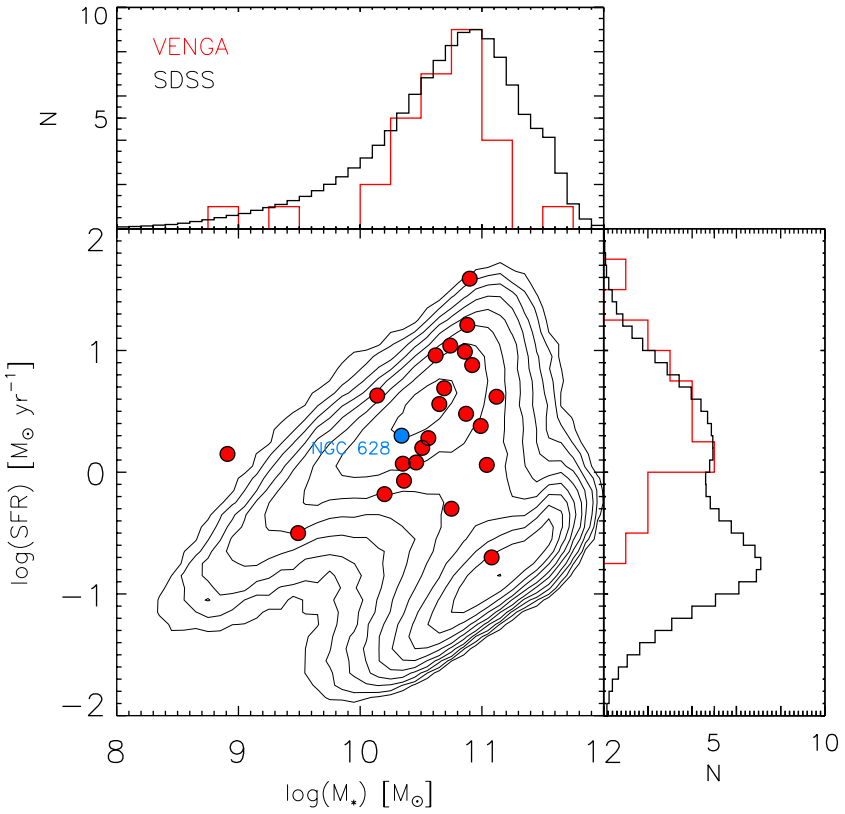

Figure 2. Stellar mass vs. star formation rate for the VENGA galaxies with SFR measurements in Table 3 (red circles), and star-forming galaxies in the SDSS MPA/JHU DR7 catalog (black contours). The red and black histograms show the distributions for the VENGA and SDSS galaxies, respectively. The stellar mass histogram includes the VENGA targets without SFR measurements. NGC 628 is shown as a blue circle.

(A color version of this figure is available in the online journal.)

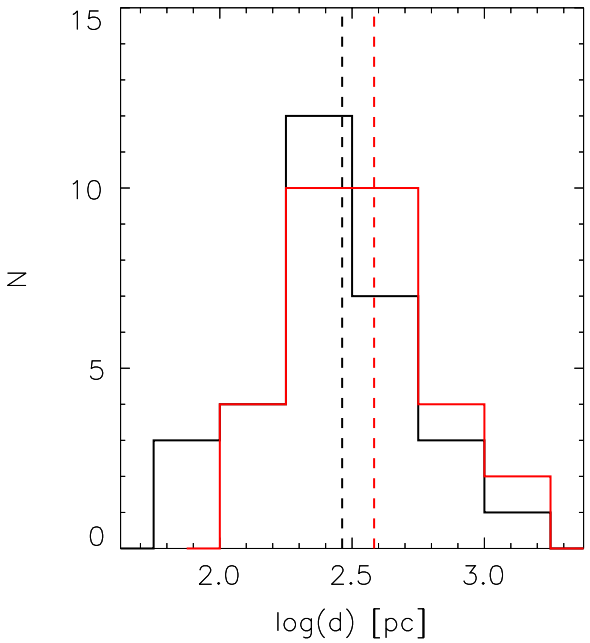

Figure 3. Histogram of the logarithm of the VIRUS-P 4.″24 fiber size in physical units for each galaxy in the VENGA sample (black), given the distances adopted in Table 1. Also shown is the size of the 5.″6 FWHM PSF of the final data cubes (red). The vertical dashed lines mark the median native and effective spatial resolutions of 290 pc and 383 pc.

(A color version of this figure is available in the online journal.)

FWHM, and are stacked vertically on the CCD at approximately 8 pixels apart from each other, minimizing cross-talk between fibers.

For each VIRUS-P pointing we observe three dithers at relative positions $(\Delta\alpha, \Delta\delta) = (0.''0, 0.''0)$, $(-3.''6, -2.''0)$, and $(0.''0, -4.''0)$ from the origin to ensure full coverage of the FOV. Therefore in each pointing we obtain spectra for 738 independent regions. Depending on the angular size of the targets we observe up to three pointings on each galaxy providing full coverage of the central part of the galaxies and a sampling of the disk of most targets out to $\sim 0.7 R_{25}$ (see Figure 1 and last column of Table 1). Overall the VENGA survey consists of 60 individual pointings composed of three dithers each, amounting to spectra of ∼44,000 independent regions (typically a few 100 pc in diameter) across the disks of the 30 galaxies in the sample.

The spectral range of VIRUS-P can be adjusted within the 3600–6800 Å window. The instrument has a set of volume phase holographic gratings that provide different spectral resolutions and wavelength coverages. For VENGA we use the lowest resolution grating (VP1), which provides a spectral resolution of ∼5 Å FWHM and coverage over a ∼2200 Å wide spectral window. We observe each galaxy in a blue setup (3600–5800 Å) and a red setup (4600–6800 Å), obtaining full spectral coverage in the 3600–6800 Å range and doubling the effective exposure time in the overlap region (4600–5800 Å). All the data are taken with 1×1 binning, which translates into a spectral dispersion of ∼1.11 Å pixel^{-1}, except for some early observations of the central pointing of NGC 5194, which were taken using 2×1 binning in the spectral direction (Blanc et al. 2009).

Table 2
Bulge Structural Parameters

Object	B/T	$n_{\rm Bulge}$
NGC 337	...	...
NGC 628	0.10[a]	1.35
NGC 1042	...	...
NGC 1068	...	...
NGC 2775	0.61[b]	4.85
NGC 2841	0.17[c]	2.97
NGC 2903	0.09[c]	0.42
NGC 3147	0.25[a]	3.66
NGC 3166	0.25[b]	0.56
NGC 3198	0.11[a]	5.12
NGC 3227	...	...
NGC 3351	0.17[c]	1.51
NGC 3521	0.10[a]	3.20
NGC 3627	0.08[c]	2.90
NGC 3938	0.07[b]	1.18
NGC 3949	...	...
NGC 4013	...	...
NGC 4254	0.39[b]	2.68
NGC 4314	...	...
NGC 4450	0.17[b]	2.26
NGC 4569	0.06[c]	1.90
NGC 4826	0.13[c]	3.94
NGC 5055	0.26[a]	1.84
NGC 5194	...	...
NGC 5713	0.33[b]	1.84
NGC 5981	...	...
NGC 6503	...	...
NGC 6946	...	...
NGC 7479	0.09[b]	1.09
NGC 7331	...	...

Notes.
[a] *K*-band decomposition, Dong & De Robertis (2006).
[b] *H*-band decomposition, Weinzirl et al. (2009).
[c] *V*-band decomposition, Fisher & Drory (2008).

Table 3
Stellar Masses and Star Formation Rates

Object	$\log(M_*)$ ($M_\odot$)	log(SFR) ($M_\odot$ yr^{-1})	Ref.
NGC 337	10.2	0.63	K03[a]
NGC 628	10.3	0.30	L09[b]
NGC 1042	8.9	0.15	T07[c]
NGC 1068	10.9	1.59	T07
NGC 2775	11.1	0.06	T07
NGC 2841	11.1	−0.70	K03
NGC 2903	10.7	0.56	L09
NGC 3147	11.5	...	...
NGC 3166	11.0	...	...
NGC 3198	10.4	−0.07	K03
NGC 3227	10.8	...	...
NGC 3351	10.0	0.20	L09
NGC 3521	11.0	0.38	L09
NGC 3627	10.7	0.69	L09
NGC 3938	10.5	0.08	K03
NGC 3949	10.3	...	...
NGC 4013	10.7	...	...
NGC 4254	11.6	1.04	K03
NGC 4314	10.7	−0.18	T07
NGC 4450	10.8	−0.30	K03
NGC 4569	10.6	0.28	K03
NGC 4826	10.4	0.07	L09
NGC 5055	10.9	0.48	L09
NGC 5194	10.9	0.88	L09
NGC 5713	10.9	0.99	T07
NGC 5981	10.9	...	...
NGC 6503	9.5	−0.50	L09
NGC 6946	10.6	0.96	L09
NGC 7479	10.9	1.21	T07
NGC 7331	11.1	0.62	K03

Notes.
[a] K03: Kennicutt et al. (2003).
[b] L09: Lee et al. (2009).
[c] T07: Thilker et al. (2007).

In terms of depth, the goal of VENGA is to obtain spectra that reach a median S/N $\sim$ 40 in continuum per spectral resolution element (FWHM) per fiber across each galaxy. For most scientific applications this high S/N per fiber requirement prevents us from having to bin our data over many spatial resolution elements, therefore ensuring good spatial resolution throughout most of the maps. Exposure times for different galaxies were scaled using their effective *B*-band surface brightness taken from the RC3 catalog (de Vaucouleurs et al. 1991; Table 1) and typically range from 45 minutes to 3 hr per dither. The three dither positions and two wavelength setups used imply effective exposure times ranging from 4.5 hr to 18 hr per pointing.

3. OBSERVATIONS

The VENGA survey is still in the phase of data acquisition. Observations of all targets in the red spectral setup started in 2008 April and were completed in 2010 July. Blue setup observations started in 2010 September and we expect them to be completed during 2013. Table 4 lists all the observing runs we have conducted as part of VENGA, the instrumental setup used, the number of nights observed, and the galaxies for which data were obtained.

As mentioned above the typical exposure times for each dither range from 45 minutes to 3 hr, typically divided in shorter 15 to 25 minute exposures. When conditions are not photometric we increase the exposure times to ensure reaching the desired depth. Because of the large angular diameter of our targets, during most observations the VIRUS-P IFU never samples regions of blank sky. Therefore, off-source sky exposures are necessary to measure and subtract the sky spectrum from the science data. We obtain 5 minute sky frames bracketing each science exposure. The off-source frames are taken 30′ north of each galaxy in fields that have been confirmed not to contain extended sources.

Bias frames, arc lamps, and twilight flats are obtained at the beginning and end of each night. For the red setup we use a combination of Ne+Cd comparison lamps and for the blue setup we use Hg+Cd. These combinations of lamps provide a good set of strong lines over the full spectral range of each setup, allowing a good wavelength calibration with minimal extrapolation toward the CCD edges.

During most nights we obtain data for one or two spectrophotometric standard stars using the six-position fine dithering pattern presented in Blanc et al. (2009). As described in Sections 4.5 and 4.6 standard stars are used to perform the relative flux calibration while the absolute flux level is calibrated against broadband images. During some observing runs the spectra of 1–3 out of the 246 fibers fell off the CCD due to camera and grating alignment problems. This translates into a lack of spectra for a few fibers in the corner of the FOV, which does not affect the data significantly.

Table 4
VENGA Observing Runs

Dates	Observed Nights	Instrumental Setup	Observed Galaxies
2008 Aug 4	1	Red	NGC 5194
2008 Nov 4–2008 Nov 9	6	Red	NGC 628, NGC 1068
2009 Jan 28–2009 Jan 31	4	Red	NGC 2903, NGC 3521
2009 Feb 1–2009 Feb 3	3	Red	NGC 1042, NGC 2775, NGC 3227, NGC 3949, NGC 4314
2009 Mar 30–2009 Apr 2	3	Red	NGC 3351, NGC 4254
2009 Apr 17–2009 Apr 19	4	Red	NGC 4254, NGC 5194
2009 Jul 15–2009 Jul 16	2	Red	NGC 5713, NGC 6503
2009 Jul 21–2009 Jul 23	1	Red	NGC 6503
2009 Sep 11–2009 Sep 15	3	Red	NGC 337, NGC 1068, NGC 5981, NGC 6503, NGC 7479
2009 Nov 9–2009 Nov 15	4	Red	NGC 628, NGC 1042, NGC 1068, NGC 2775
2009 Dec 9–2009 Dec 21	12	Red	NGC 628, NGC 1042, NGC 2775, NGC 2841, NGC 3166, NGC 3227, NGC 3521, NGC 3627
2010 Jan 11–2010 Jan 16	4	Red	NGC 1042, NGC 2841, NGC 3147, NGC 3627, NGC 4013
2010 Feb 14–2010 Feb 18	4	Red	NGC 1068, NGC 2775, NGC 3147, NGC 3198, NGC 4013, NGC 4254
2010 May 18–2010 May 20	3	Red	NGC 3998, NGC 5055
2010 Jun 4–2010 Jun 6	2	Red	NGC 3198, NGC 4450, NGC 6964
2010 Jul 5–2010 Jul 9	3	Red	NGC 4450, NGC 6946
2010 Sep 1–2010 Sep 7	6	Blue	NGC 1068, NGC 5981, NGC 6503, NGC 6946, NGC 7479, NGC 7731
2010 Oct 1–2010 Oct 6	5	Blue	NGC 337, NGC 628, NGC 1068, NGC 6946, NGC 7731
2010 Nov 10–2010 Nov 14	2	Blue	NGC 628
2010 Dec 7–2010 Dec 12	5	Blue	NGC 628, NGC 1042, NGC 2775, NGC 2903
2010 Dec 27–2011 Jan 2	5	Blue	NGC 628, NGC 2775, NGC 2841, NGC 3147, NGC 3227
2011 Jan 27–2011 Feb 2	4	Blue	NGC 628, NGC 2775, NGC 2841, NGC 3147, NGC 3166, NGC 3198, NGC 3227
2011 Feb 7–2011 Feb 10	3	Blue	NGC 2841, NGC 3147, NGC 3166, NGC 3198, NGC 3227, NGC 3521
2011 Mar 28–2011 Mar 31	4	Blue	NGC 2775, NGC 3147, NGC 3351, NGC 3627, NGC 5713
2011 Apr 8–2011 Apr 10	1	Blue	NGC 3351, NGC 3949
2011 May 4–2011 May 9	5	Blue	NGC 3227, NGC 3949, NGC 3938, NGC 5194, NGC 5055, NGC 3521, NGC 3521, NGC 4826
2011 Jun 24–2011 Jul 4	5	Blue	NGC 4254, NGC 4826, NGC 4013
2012 Mar 16–2012 Mar 22	4	Blue	NGC 3521, NGC 4013, NGC 4314, NGC 4450 NGC 4569

Table 5
Summary of VENGA Observations of NGC 628

Pointing	Equatorial Coord.		Setup	Dither	Exposure Time	N	⟨Seeing⟩	⟨Transparency⟩
	α	δ			(hr)		($''$)	
			Red	D1	4.00	12	2.06	0.87
P1	01:36:42.45	15:47:04.6	Red	D2	3.33	10	2.23	0.87
			Red	D3	3.33	10	2.20	0.89
			Blue	D1	3.33	8	2.19	0.71
			Blue	D2	2.92	7	2.06	0.64
			Blue	D3	3.33	8	1.55	0.73
			Red	D1	3.00	6	1.92	0.65
P2	01:36:49.45	15:47:04.2	Red	D2	3.50	7	2.00	0.67
			Red	D3	3.50	7	1.87	0.68
			Blue	D1	5.00	12	1.72	0.68
			Blue	D2	5.00	12	1.53	0.69
			Blue	D3	5.00	12	2.23	0.65
			Red	D1	8.50	17	2.62	0.63
P3	01:36:35.51	15:47:05.0	Red	D2	7.50	15	2.72	0.61
			Red	D3	7.50	15	2.57	0.68
			Blue	D1	5.42	13	2.27	0.49
			Blue	D2	5.42	13	2.82	0.58
			Blue	D3	4.58	11	2.18	0.58

3.1. NGC 628 Data

In this paper we present the VENGA data over three VIRUS-P pointings on the face-on Sc galaxy NGC 628. A summary of the data is provided in Table 5. Observing conditions were variable between different runs and within different nights during the same observing run, ranging from photometric to partly cloudy conditions with average atmospheric transparency down to ∼60%. The seeing (as measured from the guide star in the co-focal guider camera of the instrument) ranged between 1.″3 and 4.″0 (FWHM) with a median of 2.″0.

Table 5 presents a summary of the NGC 628 VENGA data after rejecting 12 out of 207 frames (6%) that are affected by pointing errors or catastrophic sky subtraction problems (see Sections 4.4 and 4.6). For each dither in each pointing on the galaxy we list the total on-source exposure time, the number of frames, the average seeing of the frames, and the mean atmospheric transparency (as measured in Section 4.6). Overall we obtained 84.2 hr of exposure on NGC 628, which translates into an extremely deep spectral data cube for this galaxy. The VENGA data on NGC 628 are roughly a factor of two deeper than for the typical target in VENGA.

4. DATA REDUCTION AND CALIBRATION

Data reduction is performed using the VACCINE pipeline (Adams et al. 2011) in combination with a series of custom built IDL routines. In this section we describe the data processing including the flat fielding, wavelength calibration, and sky subtraction of individual science frames, and their flux calibration (both in the relative, i.e., across wavelength, and absolute sense). We also discuss astrometric corrections applied to the data. Both the astrometry and absolute flux calibration are based on the comparison of reconstructed broadband images from the VIRUS-P IFU spectra and archival broadband images of the galaxies. Finally, we describe the method used to combine individual frames taken in different wavelength setups and at different positions in order to create the final data cubes and row-stacked-spectra (RSS) files for the VENGA galaxies. At each step in the data reduction, VACCINE and our set of external IDL routines propagate a properly calculated error frame, which is associated with each science frame and used to compute the uncertainty in the final spectra.

Throughout this section we use the NGC 628 VENGA data to exemplify the results of different procedures. We describe the processing steps in the order in which they are applied to the data.

4.1. Basic CCD Processing, Cosmic-ray Rejection, and Fiber Tracing

All individual frames (bias, flats, arcs, sky, and science) are overscan subtracted. We combine all the overscan subtracted bias files for each observing run (usually ∼100) to create an image of any residual bias structure, which is subtracted from all the flat, arc, sky, and science frames.

We use the LA-Cosmic laplacian cosmic-ray identification algorithm of van Dokkum (2001) to identify and mask cosmic rays in the science images. We tune the algorithm to be robust enough to identify most cosmic rays in the science frames while ensuring that real emission lines are not masked. Any residual cosmic rays not identified in this pass are removed from the data during the combination of multiple frames (Section 4.6).

Twilight flats are used to trace the spectrum of each fiber on the CCD. VIRUS-P is mounted on a gimbal attached to the broken Cassegrain focus of the 2.7 m telescope. The gimbal keeps the spectrograph at a constant gravity vector, making flexure effects on the optical path of the instrument negligible. Thanks to this, with VIRUS-P there is no need to obtain calibrations at the same time and telescope position of the science data. We have observed shifts in the positions of fibers on the CCD (at the 0.1 pixel level) when large changes in temperature occur. VACCINE corrects for these small offsets during the flat-fielding stage to properly remove the spatial PSF of each fiber from the two-dimensional (2D) spectra (Section 4.3). To minimize the magnitude of these temperature induced offsets we use the set of twilight flats that is closest in temperature to the average temperature at which the science data are taken for both tracing and flat fielding. Most of the time this means that the twilight flats taken at dawn are used.

We extract the 2D spectrum of each fiber in the science, sky, arc, and flat frames using a 5 pixel aperture centered around the pixel containing the centroid of the fiber's spatial profile. Using a discrete pixel instead of a fractional pixel aperture centered on the trace centroid itself avoids having to resample the data and conserves the noise properties of individual pixels. Using a fixed aperture that matches the FWHM of the fiber spatial profile implies that we recover 76% of the total flux passing through the fiber and makes the effects of neighboring fiber cross-talk negligible. We prefer to adopt this approach instead of a more sophisticated method to recover the flux in the wings of the fiber spatial profile (e.g., Gaussian Suppression; Sánchez 2006) as the potential ∼15% improvement in S/N that could be gained in the case of perfect deblending and extraction is hampered by the systematic flat-fielding uncertainty introduced by the correction of temperature induced offsets in the edges of the fiber profile.

At this stage in the reduction VACCINE constructs a formal error map that accounts for both read-noise and Poisson uncertainty for each pixel in the 2D spectrum of each fiber. These maps are properly propagated throughout the rest of the reduction (assuming Gaussian uncertainties) and end up providing the weights used when combining and collapsing spectra from different frames, as well as the flux error in the final data cube.

4.2. Wavelength Calibration and Characterization of the Instrumental Spectral Resolution

Arc lamp frames are combined to produce a master arc for each night. VACCINE is typically able to match and fit ∼12 emission lines in the blue setup lamps (Hg+Cd) and ∼20 lines in the red setup lamps (Ne+Cd). We fit the wavelength solution for each fiber independently using a fourth-order polynomial. Residuals in the wavelength solution show an rms dispersion of $\sigma_\lambda \simeq 0.1$ Å, or a tenth of a pixel (∼6 km s^{-1} at 5000 Å).

We also use the emission lines in the master arc frame to characterize the spectral resolution as a function of wavelength for each fiber. We measure the FWHM of non-blended arc lines by performing single Gaussian fits. By fitting a second-order polynomial to the measured FWHM values across the spectral direction for each fiber we create a robust map of the instrumental spectral resolution ($\mathrm{FWHM_{ins}}$) of each fiber as a function of wavelength. Good knowledge of the resolution is essential at the time of fitting galaxy spectra with linear combinations of empirical or synthetic templates that must be convolved to the same resolution of the data in order to extract meaningful line-of-sight velocity distributions (LOSVDs) from the fits.

The VIRUS-P instrumental resolution is observed to change smoothly as a function of position on the detector, with values ranging from 4.6 Å to 6.1 Å FWHM. No variation in the instrumental spectral resolution is observed between observing runs. In the final data cube of NGC 628 the median instrumental resolution in velocity units is $\sigma_{\mathrm{inst}} = 123$ km s^{-1}.

4.3. Flat Fielding

The flat-fielding process in VACCINE is used to divide out three different effects from the data: (1) the relative fiber-to-fiber throughput, (2) the profile of the fiber PSF on the detector across the spatial direction, and (3) the CCD pixel-to-pixel variations in quantum efficiency. A master twilight flat is created for each night by combining the set of flat frames closer in temperature to the average throughout the night. First, VACCINE removes the signal from the solar spectrum from the master twilight flat. For each fiber, this is achieved by fitting a B-spline to the twilight spectra of a set of 60 neighboring fibers on the chip (which share a similar spectral resolution) to create a template solar spectrum (which also includes the spectral response of the instrument), and then normalizing the spectrum of the fiber of interest by this combined high S/N template (see Adams et al. 2011). Since each fiber provides an independent wavelength sampling of the twilight spectrum, combining data from a large set of neighboring fibers effectively yields a sub-pixel sampled spectrum, which after being fit by the B-spline can be evaluated at the exact wavelength scale of the fiber of interest.

From the resulting normalized flat, VACCINE creates a "fiber profile" flat by running a median smoothing kernel across the spectral direction. This new frame contains only the relative fiber-to-fiber throughput and the fiber PSF spatial profile. Dividing the normalized flat by this smoothed version yields a pixel-to-pixel flat that is applied to the data.

As mentioned in Section 4.1, small (sub-pixel) temperature-induced offsets in the fiber positions on the CCD are sometimes present in the data. This can translate into undesired residuals when removing the spatial profile of the fibers if the data are divided by a flat field that is offset in the spatial direction. Residuals can be particularly large at the edges of fibers, where the data values are divided by smaller numbers than at the fiber core. These offsets must be corrected for, in order to remove the fiber PSF across the spatial direction. To do so, VACCINE traces each fiber in the science frame (after running a 30 pixel boxcar filter across the spectral direction to ensure a high S/N measurement of the fiber centroid), and computes an offset with respect to the same fiber centroid in the "fiber profile" flat. These offsets are used to resample the smoothed "fiber profile" flat using an optimal sinc-interpolation method in order to align it with the data. We divide the science and sky frames by this resampled smoothed flat frame, therefore removing the fiber spatial profile from the data.

4.4. Sky Subtraction

Sky spectra are measured by combining information from the two off-source sky exposures taken before and after each science frame. In Blanc et al. (2009) we simply averaged the before and after off-source frames to create the sky frame used for background subtraction. While this method worked well for the NGC 5194 data presented there, those observations were taken far from twilight and under very stable and dark conditions. We find that when conditions are not optimal (e.g., close to twilight, when clouds are present, or near moonrise or moonset) the sky brightness can change nonlinearly with time, making the simple averaging of bracketing sky frames insufficient to produce an adequate sky subtraction. We adopt a more sophisticated method to estimate and subtract the sky spectrum from our data, which makes use of the temporal information we can extract regarding the variability of the sky brightness as a function of wavelength, from all the sky frames obtained throughout a single night.

As an example, Figure 4 shows the raw (i.e., not flux calibrated) sky spectrum measured from 13 off-source sky frames taken during the night of 2008 November 7 using the red VIRUS-P setup. The spectra are color coded by UT time, with purple at the beginning of the night and red at the end of the night. We adopt the UT time corresponding to the middle of each exposure. The elevated brightness and blue color of the spectrum at the beginning of the night is due to the first-quarter moon. Moonset at McDonald Observatory on that date

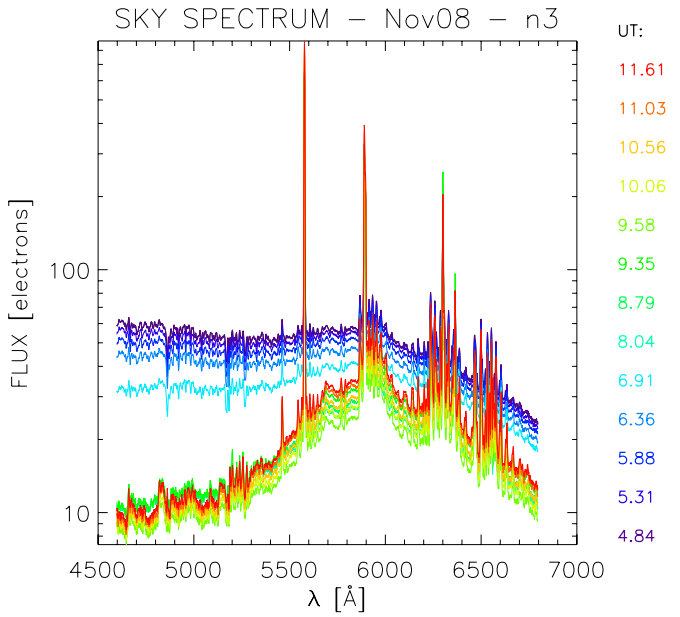

Figure 4. Sky spectrum in raw units (before flux calibration) at different UT times (color coded) during the night of 2008 November 7 for the VIRUS-P red setup.

(A color version of this figure is available in the online journal.)

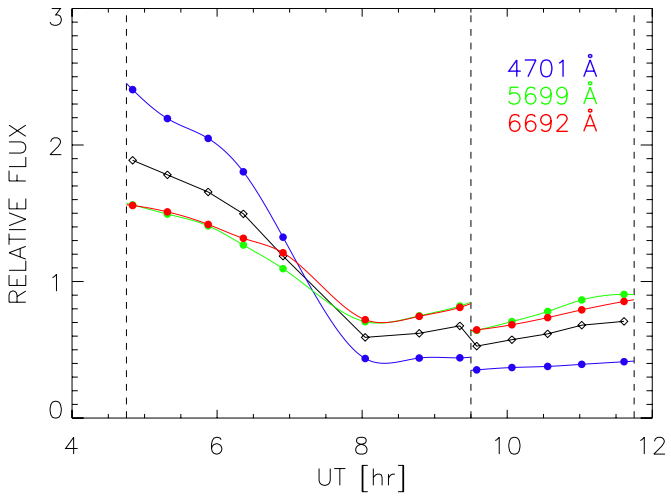

Figure 5. Relative sky brightness as a function of UT time for the same night shown in Figure 4 at three different wavelengths (blue, green, and red). Filled circles correspond to measurements of the sky brightness from the off-source background frames. The beginning and end of observations of the same target are shown as vertical dashed lines. Solid color curves show cubic spline fits to the sky brightness. The black open diamonds and black solid curve show the relative sky brightness averaged over the full spectrum.

(A color version of this figure is available in the online journal.)

occurred at 8.47 hr UT and can be clearly seen as a sharp drop in the sky brightness, particularly at blue wavelengths. For this night, the darkest skies occurred between 9 hr and 10 hr UT. These are followed by a monotonous increase in sky brightness that is steeper at redder wavelengths. This brightening and reddening is due to both the approach of twilight and the fact that the observations were being performed at increasing airmass. Our sky subtraction method uses all this information regarding the wavelength and time dependence of the sky brightness throughout each night to correct the two bracketing off-source sky exposures so that they match the sky spectrum at the time when the science frame is taken.

To trace these changes we average the spectra of all fibers in each individual sky frame and then divide this average sky spectrum into 500 wavelength bins (each corresponding roughly to a spectral resolution element). On a night-by-night basis, we use the time stamps of all sky frames to construct a nightly "light curve" of the night sky surface brightness at the central wavelength of each of these 500 bins. Figure 5 shows the relative change in sky brightness across the same night presented in Figure 4, for three different wavelength bins near the blue end, middle, and red end of the spectrum (blue, green, and red, respectively). Measurements for individual sky frames are shown as filled circles. For reference, the black open diamonds show the change in bolometric brightness (i.e., in the total flux integrated across the whole spectrum). The trends described in the last paragraph are clearly seen. At the beginning of the night the sky brightness falls more steeply in the blue than in the red as the moon sets, and rises faster in the red than in the blue as we approach twilight at the end of the night. Vertical dashed lines mark the beginning and end of observations of the same galaxy. The discontinuity in the sky brightness at these times is expected since the telescope is pointed in a different direction. We refer to each of these sections of the night as "observing blocks."

Within each individual observing block, we fit the temporal evolution of the sky brightness in each wavelength bin using a cubic spline (color solid curves in Figure 5). The best-fit splines allow us to evaluate the overall spectral shape of the sky emission at any arbitrary UT time within an observing block. This allows us to calculate a wavelength-dependent normalization curve by which the two bracketing sky frames must be multiplied in order to reconstruct the sky spectrum at the exact UT time of the science exposure. Since the normalization factors computed in the 500 wavelength bins are inherently noisy, we fit them as a function of wavelength using a fifth-order polynomial. This allows us to multiply the sky frames by a smooth function of wavelength containing the correction without introducing further noise into the observed sky spectrum. We apply this procedure to correct the before and after sky frames to the UT time of each science frame, and then average the two corrected frames to create a single sky background file associated with each science exposure. Sky subtraction is performed by VACCINE using this composite corrected sky frame.

Once this final sky frame is available, the method used by VACCINE to subtract the sky spectrum is analog to the B-spline algorithm used to remove the solar spectrum from the twilight flats (see Section 4.3). Briefly, for each fiber in the science exposure the sky spectrum of a set of neighboring fibers in the background frame is simultaneously fit using a B-spline and is then subtracted from the science fiber spectrum after scaling for the difference in exposure time between science and sky frames. As mentioned above, this procedure greatly benefits from the sub-pixel sampling of the sky obtained by combining information from different fibers having slightly different wavelength solutions.

The quality of the sky subtraction in VENGA is excellent. We typically see sky subtraction residuals that are fully consistent with Poisson plus read-noise uncertainties. Larger systematic residuals usually appear at the wavelengths of the four brightest sky emission lines in our wavelength range. These residuals are caused by the fast time variability of these spectral features, which is independent of the variability of the sky continuum and broad emission bands that dominate our corrections. These

bright sky lines are masked during the analysis of the science data. Rarely (less than 4% of the frames in the case of NGC 628), when observations are taken under extremely bad observing conditions (usually combinations of clouds and moon, or clouds and proximity to twilight), obvious residuals in the sky subtraction can be observed in the sky-subtracted science exposures. We reject these frames from the data set.

4.5. Spectrophotometric Flux Calibration

We use observations of spectrophotometric standard stars from Massey et al. (1988) and Oke (1990) to calibrate the VENGA spectra. The method used to construct sensitivity curves from the IFU observations of standard stars is described in Blanc et al. (2009). The only difference with the approach taken in that previous work is that here standard stars are only used to perform the relative flux calibration as a function of wavelength. The absolute scale of the calibration comes from a comparison to broadband optical images of the VENGA galaxies. The absolute calibration is described in the next section.

We calculate sensitivity curves for all standard stars taken during each observing run. These curves are normalized to a common scale and averaged to create a master sensitivity curve for each run. All science frames obtained during each observing run are multiplied by these curves to convert them to units of erg s^{-1} cm^{-2} $Å^{-1}$. Since the atmospheric transparency at the time of the science and standard star observations is unknown, we need the absolute scaling described in the following section. The error maps for each frame are scaled accordingly to the data. By looking at the dispersion between different sensitivity curves within each month, we estimate a typical uncertainty in the relative flux calibration of ∼8%.

4.6. Astrometry and Absolute Flux Calibration

The pointing of VIRUS-P is done using an offset guider camera that images a $4.'5 \times 4.'5$ field ∼9′ north of the IFU science field. An astrometric calibration between the two fields allows the observer to point the IFU by putting a guide star at specific pixel coordinates on the guider detector. Adams et al. (2011) found systematic offsets of the order of 1″ between the same pointings made over different observing runs. These offsets are also present in our data and must be taken into account before combining multiple frames. In order to accurately recover the astrometry of the VENGA science observations we register reconstructed broadband images of the galaxies made from the IFU data to archival broadband images. These comparisons are also used to calibrate the spectra in terms of absolute flux. For the NGC 628 blue and red IFU data we use the SDSS-III[12] DR8 *g*-band and *r*-band mosaics.[13]

For every science exposure we integrate the spectrum of each fiber over the corresponding SDSS transmission curve (*g* or *r* for blue and red setup data, respectively) in order to measure the monochromatic flux at the effective wavelength of the broadband filter. Simultaneously we convolve the SDSS image of the galaxy with a Gaussian kernel to match the PSF to the seeing under which the VIRUS-P data were taken and we perform aperture photometry at the fiducial position of each fiber. We use circular apertures that match the fiber size. After correcting the VIRUS-P fluxes for atmospheric extinction at the airmass of the observations, we compare them to the SDSS fluxes and fit them using the following expression:

$$f_{\rm SDSS} = A \times f_{\rm VP} + B, \quad (1)$$

where A is a normalization factor recovering the absolute flux scale and B recovers any residual background left from the sky subtraction process. A perfect background subtraction in both the SDSS image and the VIRUS-P spectra should translate to $B = 0$.

We perturb the fiducial astrometry of the VIRUS-P pointing by applying offsets in both right ascension and declination in order to minimize the χ^2 of the fit. This registering process provides corrected astrometry for each science frame. Given the wealth of spatial information encoded in the relative brightness of hundreds of VIRUS-P fibers, the registering is very accurate and has a typical uncertainty of ∼0.″1. The value of A at the registered position provides the absolute scale for the flux calibration and the science frame is multiplied by this value. This ties our flux calibration to that of SDSS, which has a zero-point uncertainty of 2% in the bands used here. For the 195 individual frames used to construct the NGC 628 data cube, we measure a mean $\langle B \rangle = -2 \times 10^{-18}$ erg s^{-1} cm^{-2} $Å^{-1}$ with a standard deviation of $\sigma_B = 4 \times 10^{-18}$ erg s^{-1} cm^{-2} $Å^{-1}$. This level of sky subtraction residuals corresponds to less than 2% of the median continuum level in the data and this is only an upper limit since the residuals have some contribution from the error in the SDSS sky subtraction.

Figure 6 shows the astrometric offsets that we measure for the three pointings on NGC 628 with respect to the fiducial dithering pattern. For each pointing the fiducial positions of a fiber on dithers 1, 2, and 3 are marked by black stars and solid red, green, and blue circles, respectively. Color crosses mark the actual positions at which independent science exposures were obtained. These positions are measured using the registration method described above. The black squares and dashed color circles show the average position for all exposures in each dither.

Overall the VIRUS-P acquisition accuracy is good compared to the fiber size. We observe systematic offsets from the fiducial dithering pattern in the range 0.″1–4.″0, with a mean of 1.″7. This is in good agreement with the 1.″8 accuracy found by Adams et al. (2011). As mentioned above, once the VENGA frames are registered to the broadband images and these offsets are corrected, we estimate an astrometric uncertainty of 0.″1.

When registering the data and building the final VENGA data cubes (next section) we ignore the effects of atmospheric differential refraction (ADR). At a typical observation airmass of $\chi = 1.2$ we expect less than 1″ of ADR from the blue to the red end of our data. Given the 4.″2 fiber size of VIRUS-P and the 5.″6 FWHM PSF of the final data cubes (Section 4.7), we decide not to apply an ADR correction.

To evaluate the quality of our spectrophotometric calibration we compare the VENGA spectrum of NGC 628 to the $20'' \times 20''$ long-slit driftscan spectrum obtained by Moustakas & Kennicutt (2006) as part of the ancillary data for the Spitzer Infrared Nearby Galaxies Survey (SINGS; Kennicutt et al. 2003). To do so, we use the final combined VENGA data cube described

[12] SDSS-III is managed by the Astrophysical Research Consortium for the Participating Institutions of the SDSS-III Collaboration including the University of Arizona, the Brazilian Participation Group, Brookhaven National Laboratory, University of Cambridge, Carnegie Mellon University, University of Florida, the French Participation Group, the German Participation Group, Harvard University, the Instituto de Astrofisica de Canarias, the Michigan State/Notre Dame/JINA Participation Group, Johns Hopkins University, Lawrence Berkeley National Laboratory, Max Planck Institute for Astrophysics, New Mexico State University, New York University, Ohio State University, Pennsylvania State University, University of Portsmouth, Princeton University, the Spanish Participation Group, University of Tokyo, University of Utah, Vanderbilt University, University of Virginia, University of Washington, and Yale University.

[13] http://data.sdss3.org/mosaics

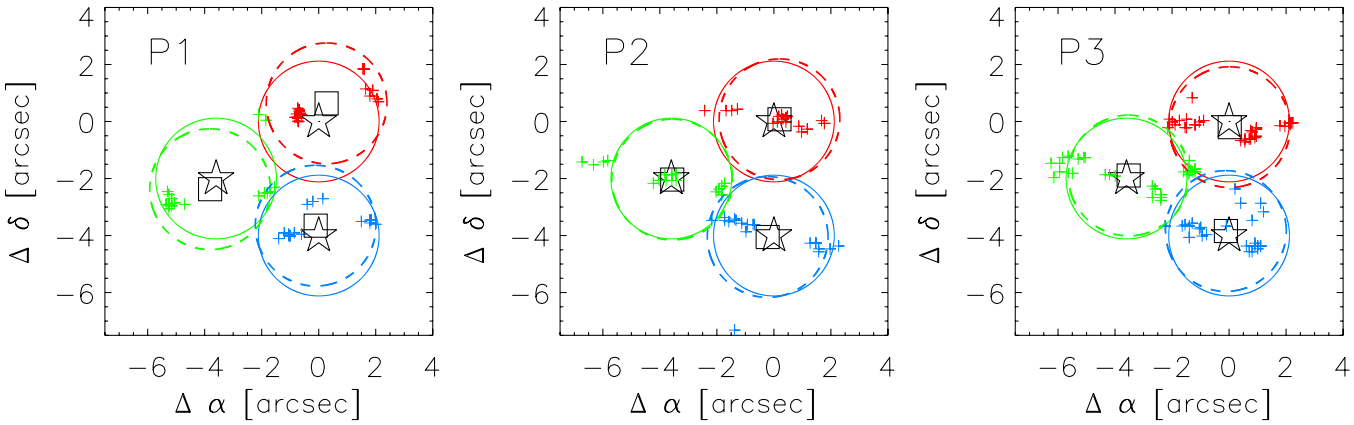

Figure 6. Attempted and actual relative positions of the three sets of dithered exposures for the three pointings obtained on NGC 628. Stars and solid circles mark the attempted fiducial positions for dithers 1, 2, and 3 (red, green, and blue, respectively). Crosses mark the actual position at which each exposure was obtained. Open squares and dashed color circles show the average fiber position of the actual observations.

(A color version of this figure is available in the online journal.)

in the following section. We integrate the IFU spectra over the same $20'' \times 20''$ region sampled by the SINGS long-slit driftscan.

The comparison is shown in the top panel of Figure 7. We observe an 18% offset between the two spectra. This offset is produced by contamination from the wings of a bright foreground star that falls slightly outside the SINGS driftscan box but which significantly contributes to the flux inside the box at the 5.″6 resolution of the VENGA data cube. Masking the contaminated spaxels (see Section 6.1) brings the VENGA and SINGS spectra into agreement. Except for regions on top of strong emission and absorption lines, where residuals arising from differences in spectral resolution dominate, both spectra show less than 5% deviations from each other over 80% of the overlap spectral range, rising toward the 10% level at the blue end of the spectrum. This is well within the 10%–30% uncertainty in the absolute calibration and the 3%–4% uncertainty in relative flux calibration of the SINGS spectrum as estimated in Moustakas & Kennicutt (2006), and the 8% relative flux error in the VENGA data (derived from the dispersion between different sensitivity curves in Section 4.5).

To further test the quality of the VENGA flux calibration we compute broadband monochromatic fluxes from the integrated spectrum over the full VENGA data cube and compare them to the flux measured over the same area in both the SDSS *g*- and *r*-band images, and the SINGS *B*- and *V*-band optical ancillary images.[14] The SINGS images are independent of our flux calibration. As shown in the bottom panel of Figure 7, the VENGA data agree with the flux measured in all four images within the quoted uncertainties. From these tests we conclude that the accuracy of the VENGA absolute and relative flux calibrations is good.

4.7. Final Combined Data Cubes and RSS Files

At this stage in the data reduction process we have a reduced, sky-subtracted wavelength and flux-calibrated 2D spectrum of each fiber (and its associated 2D error spectrum) in every individual science exposure. By 2D spectrum we mean a non-collapsed spectrum of the fiber PSF on the detector, which contains no spatial information about the source, given the fact that optical fibers scramble the input light. Also, the position of each fiber on the sky is known to 0.″1 accuracy thanks to the registering process described in the last section.

Here we describe the methods used to extract and combine data from different exposures into a final data cube containing a 1D spectrum at each position on the sky. We also describe the construction of our final RSS[15] files. These multi-extension FITS[16] files are described below and contain the spectrum and error spectrum, as well as the J2000 equatorial coordinates for each spaxel in the data cube. Also contained in the RSS file is information regarding the central wavelength and spectral instrumental resolution for every pixel in the spectra.

Data from different nights and observing runs have independent wavelength solutions. Therefore, before combining we need to resample all the spectra to a common wavelength grid. In VENGA we produce two versions of the same data cube, one with a regularly spaced linear sampling of wavelength and another with a regular logarithmic sampling (i.e., spaced regularly in velocity space). The *linear* version has pixels spaced by 1.1 Å (similar to the average dispersion in the original data), while the *logarithmic* data cubes have pixels that are spaced by $(\Delta\lambda/\lambda)c = 60$ km s^{-1}. We work with spectra in flux density units so total flux is properly conserved when resampling.

The reason behind producing two versions of the data is that while most users will be interested in using the *linear* version for many applications, the spectral fitting software used in the following section to extract stellar and gas kinematics, as well as emission line fluxes, requires input spectra that is regularly sampled in velocity space. Instead of interpolating the spectra to a linear grid for the effects of combining, and later re-interpolating the combined spectra to a logarithmic scale, we perform both resamplings directly from the original data. In this way we avoid the effects of S/N degradation associated with extra interpolations.

For each fiber in each science frame, after resampling the 2D spectra we have 5 pixels at any given wavelength that provide a measurement (with its associated error) of the flux density at a certain position on the sky. We then define a regularly spaced spatial grid of spaxels. The grid has a spaxel scale of 2″ chosen to roughly Nyquist sample the final data cube PSF. For every spaxel in the grid we compute the final spectrum by combining

[14] http://irsa.ipac.caltech.edu/data/SPITZER/SINGS/

[15] RSS files, in which every row contains the spectrum of a spaxel, should be distinguished from data cubes, as they are two-dimensional instead of three-dimensional representations of IFU data. They must be accompanied by a position table for all spaxels in order to allow for a geometrical reconstruction of the data.

[16] Flexible Image Transport System.

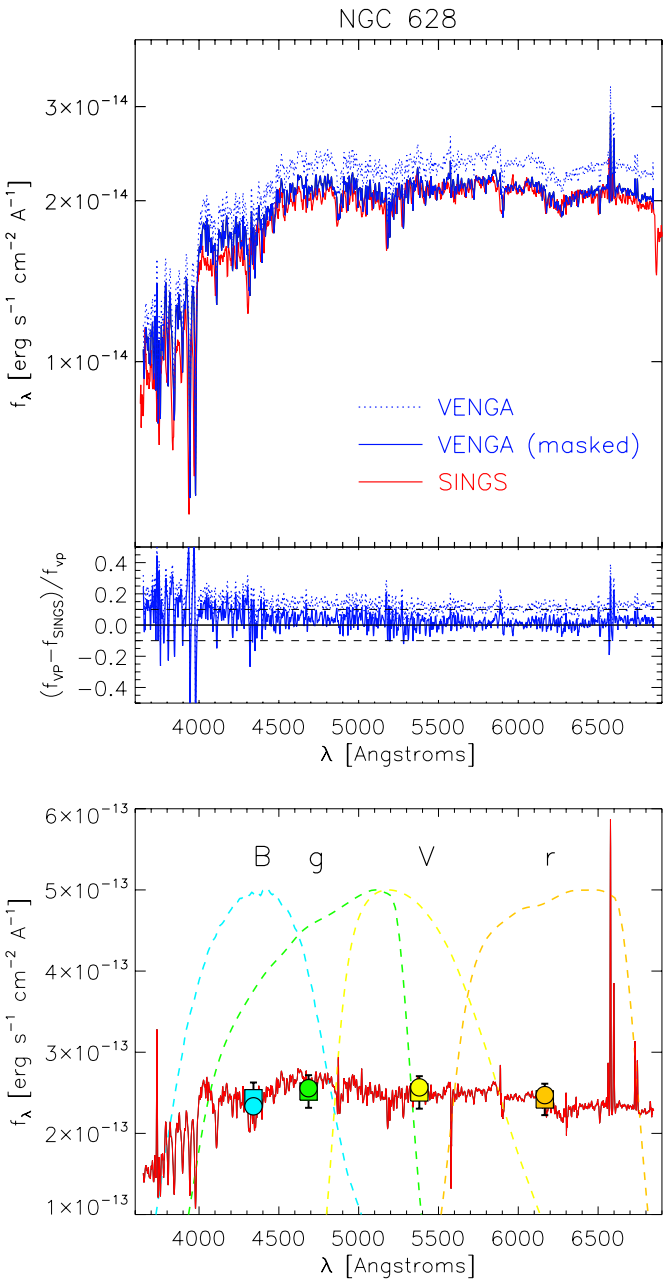

Figure 7. Top panel: comparison between the SINGS driftscan spectrum of the central 20″ × 20″ of NGC 628 (red; Moustakas & Kennicutt 2006) and the VENGA IFU spectrum (dotted blue) integrated over the same region. The solid blue curve shows the VENGA spectrum after masking a foreground star, which contaminates the measurement. Also shown are the residuals between the SINGS and VENGA spectra. Horizontal dashed lines mark a ±10% deviation. Bottom panel: comparison between the monochromatic broadband fluxes measured from the integrated VENGA spectrum over the whole data cube (squares) and the SDSS *g* and *r* and SINGS *B*- and *V*-band images (green, orange, light blue, and yellow circles, respectively). Error bars indicate the 8% uncertainty in the relative flux calibration. Also shown for reference are the integrated VENGA spectrum (red) and the broadband transmission curves (dashed lines).

(A color version of this figure is available in the online journal.)

the spectra of surrounding fibers using a Gaussian spatial filter and adopting an inverse variance weighting scheme. Therefore, the spectrum of each spaxel in the data cube is given by

$$f_\lambda(\lambda) = \frac{\sum_{i,j,k} w_{i,j,k}(\lambda) f_\lambda^{i,j,k}(\lambda)}{\sum_{i,j,k} w_{i,j,k}(\lambda)}, \quad (2)$$

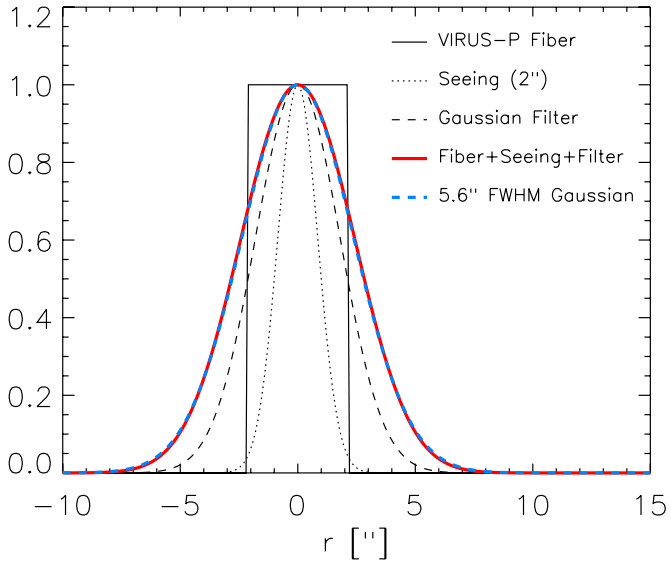

Figure 8. Final PSF of the VENGA data cubes given by the convolution of the fiber profile (solid black line) with the seeing (dotted black line) and the Gaussian spatial filter used to combine the individual exposures (dashed black line) is shown in red. The PSF is well described by a Gaussian PSF with 5.″6 FWHM (dashed blue line), and is largely independent of the seeing.

(A color version of this figure is available in the online journal.)

where $f_\lambda^{i,j,k}(\lambda)$ is the flux density of pixel k (k = 1–5) at wavelength λ of fiber j in frame i, and the weights $w_{i,j,k}$ are given by

$$w_{i,j,k}(\lambda) = \frac{1}{(\sigma_{i,j,k}(\lambda))^2} \times e^{\frac{-d_{i,j}^2}{2\sigma_g^2}}, \quad (3)$$

where $\sigma_{i,j,k}(\lambda)$ is the error in the flux, $d_{i,j}$ is the distance in arcseconds between the fiber center and the spaxel in question, and σ_g is the width of the spatial Gaussian filter used to combine the data. We use a value of $\sigma_g = 4.24/2.355$, which matches the fiber size to the FWHM of the Gaussian filter. The sum in Equation (2) is performed over all fibers within a maximum distance of the spaxel of interest. This distance cut is given by a 99% drop in the Gaussian filter weight. During the combination process we apply 3σ clipping rejection to remove any cosmic rays that were not masked by LA-Cosmic in Section 4.1. The final spatial PSF of the data cube is given by the convolution of the top-hat 4.″24 diameter fiber profile with the seeing (2.″0 FWHM for the NGC 628 data) and the 4.″24 FWHM Gaussian spatial filter used to combine the data. Figure 8 presents these three components and the product of their convolution (red solid line). The final PSF is well described by a 5.″6 FWHM Gaussian and is largely independent of the seeing. Direct measurement of the FWHM of bright foreground stars in the NGC 628 data cube empirically confirms the value of 5.″6.

As mentioned in Section 4.2, the instrumental spectral resolution at different wavelengths, for each fiber, is extracted from the arc lamps. To create a spectral resolution map for the data cube, we combine the master arc lamp frames associated with each individual science frame in the same way as the science data (i.e., using the same weights). We then use the method described in Section 4.2 to create a map of the instrumental spectral resolution from this combined arc.

The final VENGA data products for each galaxy are a data cube (used mostly for visualization purposes) and an RSS file (used for spectral fitting and analysis). The data cube consists of a multi-extension fits file, in which each extension corresponds

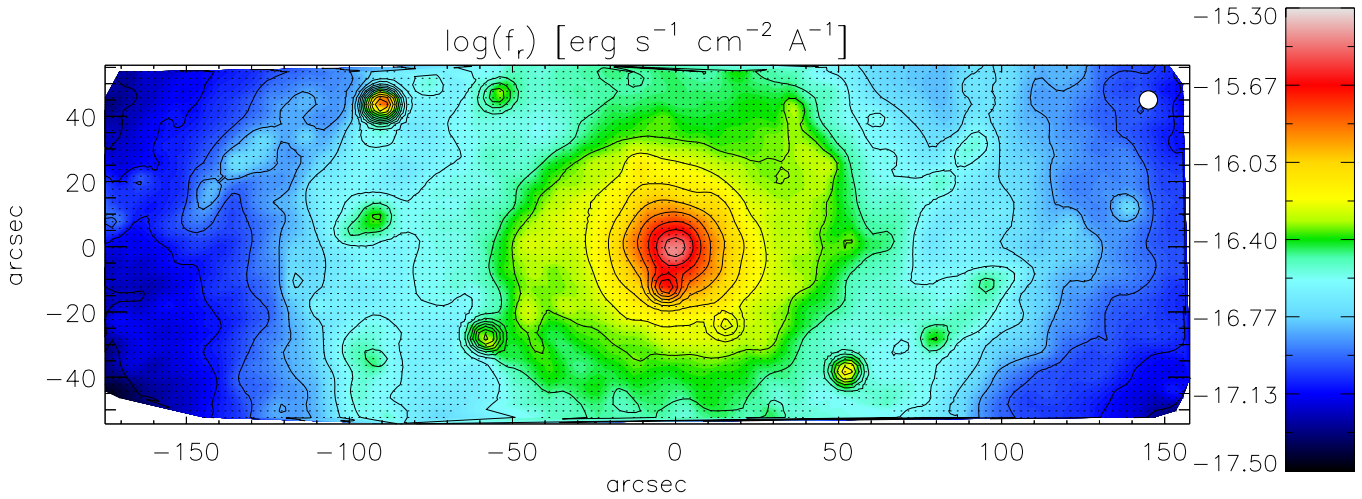

Figure 9. Map of the *r*-band flux reconstructed from the VENGA spectral data cube of NGC 628. Black contours show isophotes in the SDSS *r*-band image of the galaxy (PSF matched to the 5.″6 FWHM PSF of the VENGA data, which is shown by the white circle in the top right corner). Black dots mark the position of each spaxel in the data cube. This and all maps presented in this work were constructed using the PLOT_VELFIELD IDL routine written by Michele Cappellari (http://www-astro.physics.ox.ac.uk/∼mxc/idl/).

(A color version of this figure is available in the online journal.)

to an image of the galaxy at a given wavelength (sampled at either linear or logarithmic steps as described above). The data cubes are in units of flux density (erg s^{-1} cm^{-2} Å^{-1}).

The corresponding linear and logarithmically sampled VENGA RSS files are stored as multi-extension FITS files, and contain the following information in their different extensions:

1. Flux density spectrum for each spaxel in units of erg s^{-1} cm^{-2} Å^{-1}.
2. Error spectrum for each spaxel in units of erg s^{-1} cm^{-2} Å^{-1}.
3. Central wavelength of all pixels in the spectrum of each spaxel in units of Å.
4. Right ascension and declination of each spaxel in units of decimal degrees.
5. Instrumental spectral resolution (FWHM) as a function of wavelength for each spaxel in units of Å.

The final VENGA data cube of NGC 628 covers an area of 5.′2 × 1.′7 and samples the disk of this galaxy out to 8 kpc ($0.6R_{25}$). Figure 9 shows an *r*-band image of NGC 628 reconstructed from the final VENGA data cube. All maps presented in this paper have north pointing up and east pointing left. Black dots mark the position of each spaxel in the data cube and the white circle on the top right corner shows the PSF FWHM. The final combined spectra was integrated over the SDSS *r*-band transmission curve to create this map. For comparison, isophotal contours from the SDSS *r*-band image (with the PSF degraded to 5.″6) are overlaid in black. The similarity between the two surface brightness distributions confirms that the flux calibration and astrometric correction of the individual science frames has been done properly. The spectra in the final data cube of NGC 628 have a median S/N = 117 in the continuum per spectral resolution element (FWHM). In the central parts of the galaxy we typically have S/N > 300, while the spectra in the faintest regions have S/N ∼ 12. In terms of surface brightness depth, the NGC 628 data reach a 5σ detection limit for the continuum at a *V*-band surface brightness of 25.0 mag arcsec^{-2} (AB). We remind the reader that the data on NGC 628 are about a factor of two deeper than for the average VENGA target.

5. SPECTRAL ANALYSIS PIPELINE

In order to extract emission line fluxes, gas and stellar kinematics, and information about the stellar populations present in different parts of the galaxies, we fit the VENGA spectra using a linear combination of templates convolved with an LOSVD plus a set of Gaussian emission line profiles. To do the fitting we use the pPXF (Cappellari & Emsellem 2004) and GANDALF (Sarzi et al. 2006) IDL routines developed for this purpose by the SAURON team. In this section we describe the fitting process and present an example fit in the NGC 628 data cube. We also discuss how the uncertainty in the fitted parameters is calculated. In this paper we fit the stellar continuum using empirical stellar templates (Section 5.1). The same type of fitting can be performed using stellar population synthesis (SPS) templates to extract information about the stellar populations present in different regions within the galaxies. The SPS fitting of the VENGA galaxies will be presented in a future publication. Before fitting the spectra, the data are corrected for Galactic extinction, adopting a Milky Way (MW) extinction law as parameterized by Pei (1992), and extinction values from the maps of Schlegel et al. (1998) ($E(B-V)_{\rm MW} = 0.07$ mag or $A_{V,\rm MW} = 0.23$ mag for NGC 628).

5.1. Stellar Kinematics

We mask the spectrum of each spaxel around regions affected by sky subtraction residuals due to bright sky lines, regions potentially affected by the nebular emission lines listed in Table 6, and the edges of each of the individual instrumental setups (red and blue). We then fit for the stellar line-of-sight velocity (v_*) and velocity dispersion (σ_*) with the pPXF software, which uses the "penalized pixel" fitting technique (Cappellari & Emsellem 2004) to fit the spectrum as a linear combination of templates convolved with an LOSVD. Although the software uses a Gauss-Hermite polynomial LOSVD, and allows for the fitting of high-order terms (h_3, h_4), for the data presented here we only fit for the first two moments v_* and σ_*.

The logarithmically sampled RSS files are used as input for pPXF, which requires the spectra to be regularly sampled in velocity space. We use the MILES stellar library version 9.1

Table 6
Fitted Emission Lines in NGC 628

Transition	Wavelength (Å)	Median S/N	Fraction—5σ	Fraction—3σ
[O II][a]	3726.03	16.4	0.99	1.0
[O II][a]	3728.73	...	...	...
[Ne III]	3868.69	1.3	<0.01	<0.01
[Ne III]	3967.40	0.7	<0.01	<0.01
H8	3889.06	2.0	0.13	0.27
Hϵ	3970.08	2.7	0.18	0.42
Hδ	4101.73	3.0	0.26	0.44
Hγ	4340.47	8.0	0.74	0.89
[O III]	4363.15	0.9	<0.01	<0.01
He II	4685.74	0.4	<0.01	<0.01
Hβ	4861.32	23.5	0.97	0.99
[O III]	4958.83	3.4	0.24	0.58
[O III]	5006.77	9.5	0.89	0.98
[N I][a]	5197.90	1.9	0.01	0.15
[N I][a]	5200.39	...	...	...
[N II]	6547.96	11.3	0.92	0.98
Hα	6562.80	47.4	1.00	1.00
[N II]	6583.34	26.2	0.99	1.00
[S II]	6716.31	16.5	0.98	1.00
[S II]	6730.68	10.4	0.88	0.97

Note.
[a] Since we cannot resolve the [O II] λ3727 and [N I] λ5200 doublets, we report the median S/N and fraction of the observed area in which the lines are significantly detected for the sum of the two doublet components.

(Sánchez-Blázquez et al. 2006; Falcón-Barroso et al. 2011) as a source of empirical templates. A subset of 48 stars spanning a wide range in spectral types (O through M), luminosity classes (I through V), and metallicities ($-2 <$ [Fe/H] < 1.5) is used. Also included in the subset are horizontal branch and asymptotic giant branch stars.

Before fitting, the templates are resampled to the wavelength scale of the data. We match the spectral resolution of all spaxels in the VENGA data and the templates to the worst instrumental resolution at any given wavelength in the data cube by convolving the spectra using a running Gaussian kernel with a wavelength-dependent width. This translates in a spectral resolution of $\sigma_{\rm ins} = 110$ km s^{-1} in the red edge and $\sigma_{\rm ins} = 200$ km s^{-1} in the blue end of the spectrum. The median instrumental resolution across the convolved data cube is $\sigma_{\rm ins} = 150$ km s^{-1}. To convolve the templates we assume the corrected MILES library intrinsic resolution of 2.54 Å (Beifiori et al. 2011).

Close inspection of fits to very high S/N spaxels in the data cube (S/N $\geqslant$ 100) shows systematic residuals caused by template mismatch at the 1% level in the 5000 Å–6800 Å region, and rising up to 2% toward the blue end of the wavelength range. It is important to include this systematic uncertainty floor during the fitting process, particularly for high S/N spectra where it becomes the dominant source of discrepancy between the best-fit models and the data. We assume a systematic uncertainty of 2% at 3600 Å, linearly decreasing toward 1% at 5000 Å and staying flat at this level redward. We add this uncertainty in quadrature to the photometric errors before fitting the spectra.

In order to account for the effect of dust extinction on the shape of the continuum as well as systematic differences in the flux calibration of the data and the templates, during the minimization we fit both additive and multiplicative low-order Legendre polynomials. The low order of the polynomials prevents them from introducing features on small scales of the order of the instrumental resolution. The polynomials only match the large-scale (~100 Å) shape of the continuum in the linear combination of stellar templates and the data and they do not affect the fitting of individual spectral features.

We fit the spectrum of each spaxel individually and store the kinematic parameters (v_*, σ_*). We limit the wavelength range to the Mg I *b* absorption feature (5100–5300 Å) for the purpose of extracting the stellar velocity dispersion. We do this to avoid a systematic overestimation of σ_* caused by the broad wings of Balmer absorption lines, which are subject to rotation and pressure broadening. As discussed below, this effect is particularly significant in the spectra of star-forming regions, which have a large contribution from A-type stars. We also experiment with using other strong absorption features like Ca H+K and the *G* band, finding that Mg I *b* provides a better agreement with the published high-precision measurement of the velocity dispersion profile of NGC 628 by Herrmann & Ciardullo (2009; see Section 6.4) while the other features always produce systematically higher values of σ_*. Issues regarding the overestimation of σ_* when using Balmer lines, Ca H+K, and the *G* band have been extensively discussed in the literature (e.g., Kormendy & Illingworth 1982; Bernardi et al. 2003; Greene & Ho 2006). The instrumental resolution in the convolved spectra at the Mg I *b* feature is $\sigma_{\rm ins} = 145$ km s^{-1}.

We also perform a second fit using the full wavelength range to estimate v_*. Our simulations show that while the best-fit σ_* is biased when using the full spectrum, the best-fit v_* is not and the uncertainty in its value is reduced significantly by using the full wavelength range. After fitting, we keep the LOSVD parameters fixed over the next fitting iteration (Section 5.3), in which we also fit for the emission lines in the spectrum. Kinematic maps of NGC 628 are presented in Section 6.

5.2. Error Estimation for LOSVD Parameters

To estimate the uncertainty in the best-fit LOSVD parameters (v_* and σ_*) we fit a series of Monte Carlo realizations of simulated spectra with different stellar velocity dispersion, S/N, and combinations of stellar templates. To construct the simulated synthetic spectra we start with the best-fit linear combination of stellar templates for three different regions in NGC 628 chosen to sample an old stellar population with a spectrum dominated by K giants (taken from the central part of the galaxy), a bright star-forming H II region on a spiral arm, and a region showing a post-starburst spectrum dominated by A-type stars. The three simulated spectra are convolved with Gaussian LOSVDs having $\sigma_{*,\rm true} = 10$, 25, 50, 100, 200, 300, and 500 km s^{-1}. Gaussian noise is artificially added to the spectra, creating 40 Monte Carlo realizations of each at S/N levels per resolution element (FWHM) of 25, 50, 100, and 200.

We fit the synthetic spectra using the same methods used for the data and described in the previous section. Even though the simulated spectra do not contain emission lines, we mask the same regions that we censored when fitting the science data in order to match the available spectral information. In an attempt to account for the effects of template mismatch we remove the templates used to create the synthetic spectra from the list of templates used to fit them. The large number of templates used (~50) allows us to do this without the worry of a particular stellar type not being represented in the remaining template subset. We present results for two fits, one using the full available spectral range, and one limited to the 5100–5300 Å region around the Mg I *b* feature.

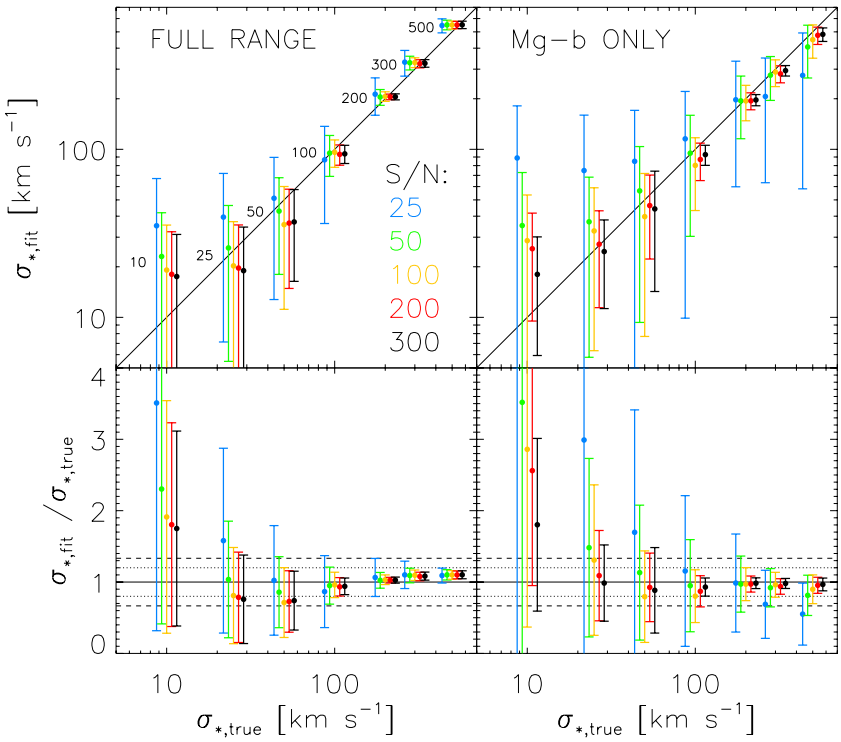

Figure 10. Top panel: comparison between the measured ($\sigma_{*,\rm fit}$) and the input ($\sigma_{*,\rm true}$) velocity dispersion from fits to Monte Carlo realizations of simulated spectra. Colors indicate the S/N of the synthetic spectra. Groups of data points for different values of $\sigma_{*,\rm true}$ are labeled in the upper left panel. Filled circles and error bars indicate the mean and standard deviation of the recovered values from 40 Monte Carlo realizations. Points are shifted by small amounts along the horizontal axis for clarity. Bottom panel: ratio between the recovered and input velocity dispersions. Dotted and dashed horizontal lines mark 20% (5σ measurement) and 33.3% (3σ measurement) deviations, respectively.

(A color version of this figure is available in the online journal.)

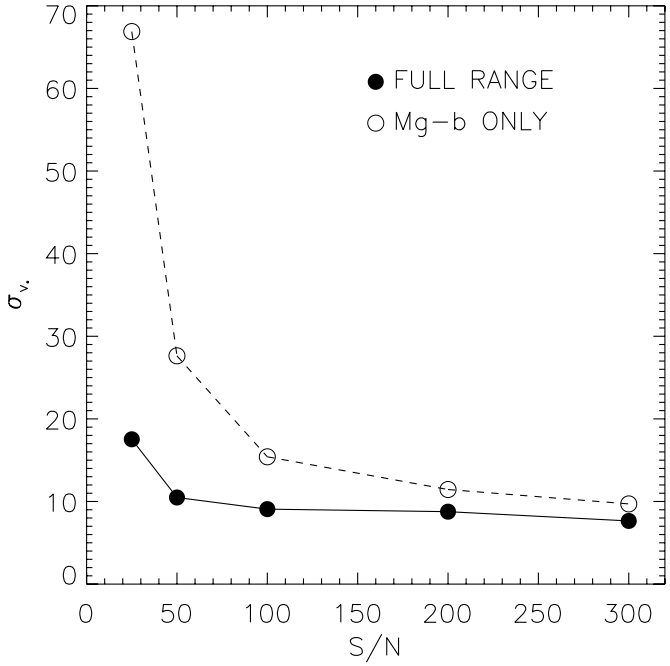

Figure 11. Error (standard deviation) in the recovered stellar velocity for fits to simulated spectra with $\sigma_{*,\rm true} < 100$ km s^{-1} as a function of signal-to-noise ratio. Filled and open circles correspond to fits using the full spectral range and fits limited to the 5100 Å–5300 Å window, respectively.

The results of the simulation are presented in Figures 10 and 11. In Figure 10 we compare the input and recovered values for the velocity dispersion at different S/Ns. In Figure 11 we present the error in the recovered radial velocity as a function of S/N for all the simulated spectra with $\sigma_* < 100$ km s^{-1} (typical of spiral galaxies). Results for fits using both the full spectral range and the limited 5100 Å–5300 Å window are reported.

When using the full spectral range the recovered stellar velocity dispersions are overestimated by ∼10% at $\sigma_{*,\rm true} > 100$ km s^{-1}, become underestimated by ∼30% below that value, and then become largely overestimated for values of $\sigma_{*,\rm true}$, which are about a factor of 10 smaller than the instrumental resolution. In the case of the full spectral range fit these trends are almost independent of the S/N. As can be seen in the right panel of Figure 10, limiting the spectral window to the Mg I *b* region removes most of these systematic deviations at the cost of larger random error bars on the recovered σ_* values. Systematic deviations are still seen at low S/N and low $\sigma_{*,\rm true}$. Balmer lines play a significant role in introducing the systematic deviations seen in the full spectral range case as is confirmed by the fact that the effect is stronger for the "star-forming" and "post-starburst" spectrum than it is for the "old stellar population" spectrum. No significant difference is seen on the recovered velocity dispersions for the three different types of spectra once the wavelength range is limited to the Mg I *b* feature.

An effect of limiting the spectral window is an increase in the random error in the recovered value of σ_*. This increase is expected because of the high EW of the rejected Balmer absorption lines. The error in σ_* for each spaxel in the data cube is computed by linear interpolation of the measured errors in the simulation to the spaxel's S/N and σ_*.

The radial velocity is recovered with no systematic deviations. Considering all simulated spectra with $\sigma_{*,\rm true} < 100$ km s^{-1} (typical of the disks of spiral galaxies) and at all the S/Ns probed, we measure mean offsets of -3 ± 11 and -2 ± 15 km s^{-1}

for the fits using the full spectral range and the 5100 Å–5300 Å window, respectively. The error in the recovered radial velocity depends on S/N as shown in Figure 11 and it is reduced by about a factor of two at the typical S/N of the data by using the full spectral range including the strong Balmer lines. The improvement is even more dramatic at low signal-to-noise (S/N $<$ 50), where the Mg triplet starts to get lost in the noise while the Balmer lines can still be easily seen in the spectra. Errors in v_* for each spaxel are computed from the S/N by linear interpolation of the simulation results (black line in Figure 11), and adding in quadrature the wavelength solution rms of 6 km s^{-1} (Section 4.2).

5.3. Emission Line Fluxes and Ionized Gas Kinematics

After measuring the LOSVD of each spaxel we use GANDALF to fit the spectrum including the emission lines. GANDALF recomputes the weights given to the different stellar templates at the same time of adding Gaussian profiles to model the contribution from emission lines. We attempt to fit all the transitions listed in Table 6.

During this fit the stellar LOSVD computed in the previous section is held fixed, but the emission line velocities, velocity dispersions, and amplitudes, as well as the weights given to the stellar templates, are free parameters. While in principle we could fit the kinematics of different lines independently, this becomes very hard for faint transitions detected at low S/N. Therefore we tie the kinematics of all emission lines to a common set of parameters ($v_{\rm gas}, \sigma_{\rm gas}$) during the fit. This ensures that the kinematic parameters are dominantly constrained by the brightest emission lines in the spectrum (typically Hα, [O III] λ5007, and [O II] λ3727). In this second iteration we also use additive and multiplicative Legendre polynomials to match the continuum shape.

Figure 12 presents the observed and best-fit spectrum of a randomly selected spaxel in the data cube. This spectrum provides a good representation of the quality of our fits. The observed spectrum is shown in blue, with photometric errors marked by the cyan envelope, and total errors (photometric plus systematic) shown as a green envelope. The solid red line is the best-fit stellar plus emission line spectrum and the dotted red line shows the best-fit stellar spectrum alone. The vertical cyan bands represent regions masked around sky line residuals and the ends of the blue and red setup spectra. Also shown are zoomed-in windows around relevant spectral features. Overall GANDALF produces fits to the VENGA spectra of excellent quality.

5.4. Errors in Emission Line Parameters and Kinematics

GANDALF returns emission line parameter errors based on the covariance matrix computed during the nonlinear Levenberg–Marquardt fitting. Therefore, the quality of this error estimates depends critically on the uncertainty in the observed spectrum being properly estimated. In particular for low EW emission lines detected in very high S/N spectra, for which the formal photometric errors are small, the inclusion of the systematic uncertainties associated with template mismatch (described in Section 5.1) is crucial in order to obtain adequate emission line flux errors. If this floor of systematic uncertainty is not included, errors in the measured emission line parameters can be significantly underestimated.

Figure 13 shows maps of the flux of the Hα, Hβ, [O II] λ3727, [O III] λ5007, [N II] λ6584, and [S II] λ6716 lines across NGC 628. We only show spaxels in which the line is detected with a significance higher than 3σ. The Hα line is detected at 5σ over the full data cube. The nebular emission clearly traces the two main spiral arms of the galaxy where ongoing star formation gives rise to prominent H II regions. In the interarm regions we still detect significant amounts of Hα emission, though with a surface brightness that is one to two orders of magnitude fainter than in the arms. A large fraction of this emission arises from the DIG component of the galaxy's ISM and is enhanced in low ionization ratios like [S II]/Hα and [N II]/Hα (Mathis 2000; Haffner et al. 2009; Blanc et al. 2009). Also clearly seen in Figure 13 is a circumnuclear star-forming ring with a diameter of ~0.5 kpc and a Hα hole in the center of the galaxy. These features and their physical origin will be discussed in a future paper.

For each transition in Table 6 we report the median S/N over all spaxels in the data cube and the fraction of the observed area in which the emission line is detected at 5σ and 3σ. Our data on NGC 628 reach a 5σ line flux limit per spaxel (4 arcsec^2) of $\sim 2 \times 10^{-17}$ erg s^{-1} cm^{-2}.

As mentioned above, we detect Hα at 5σ over the full data cube with a median S/N = 47. Other transitions are usually detected at lower significance than Hα. Individual members of the [N II] $\lambda\lambda$6548, 6583 and [S II] $\lambda\lambda$6717, 6731 doublets as well as Hγ, Hβ, [O III] λ5007, and the blended [O II] $\lambda\lambda$3726, 3729 doublet are detected at 3σ over more than ~90% of the observed area, and the [O III] λ4959 line is detected at 3σ over 58% of the area.

5.5. Nebular Extinction from Balmer Decrement

For the typical extinction regimes found in spiral galaxies the Hα to Hβ flux ratio (a.k.a. Balmer decrement) provides a good estimate of the amount of dust extinction in the regions giving rise to the nebular emission (see discussion in Blanc et al. 2009). Assuming an intrinsic Hα/Hβ ratio of 2.87 for Case B recombination in $n = 10^2$ cm^{-3}, $T = 10^4$ K gas (Osterbrock & Ferland 2006), the observed ratio provides the amount of dust reddening by means of the following relation:

$$E(B-V) = \frac{-2.5 \log\left(\frac{[\mathrm{H}\alpha/\mathrm{H}\beta]_{\rm obs}}{2.87}\right)}{k(\lambda_{\mathrm{H}\alpha}) - k(\lambda_{\mathrm{H}\beta})}, \quad (4)$$

where $[\mathrm{H}\alpha/\mathrm{H}\beta]_{\rm obs}$ is the observed line ratio and $k(\lambda)$ is the extinction law. We assume a foreground MW extinction law as parameterized by Pei (1992). SMC and LMC laws were tested (also using the Pei 1992 parameterization), and no significant change was observed in the derived extinction values (these three extinction laws are practically identical at optical wavelengths).

Figure 14 presents a map of $E(B-V)$ across the disk of NGC 628. Errors in the measured values of $E(B-V)$ are computed by propagating the uncertainty in the Hα and Hβ line fluxes. In Figure 14 we have masked regions in which the error in $E(B-V)$ is larger than 0.2 mag, which roughly amounts to an uncertainty of ~50% in the extinction correction factor at the wavelength of Hα. Regions of high extinction follow the inner rims of the spiral structure (as traced by Hα), and a visual comparison to CO maps of NGC 628 (Leroy et al. 2008) shows almost perfect coincidence between high dust extinction and high molecular gas surface density regions. Also presented in Figure 14 is a map of Hα after correcting for dust extinction. The Balmer decrement method implies a median extinction across all regions with good $E(B-V)$ measurements of $A_V = 1.06$ mag (assuming $R_V = A_V/E(B-V) = 3.1$).

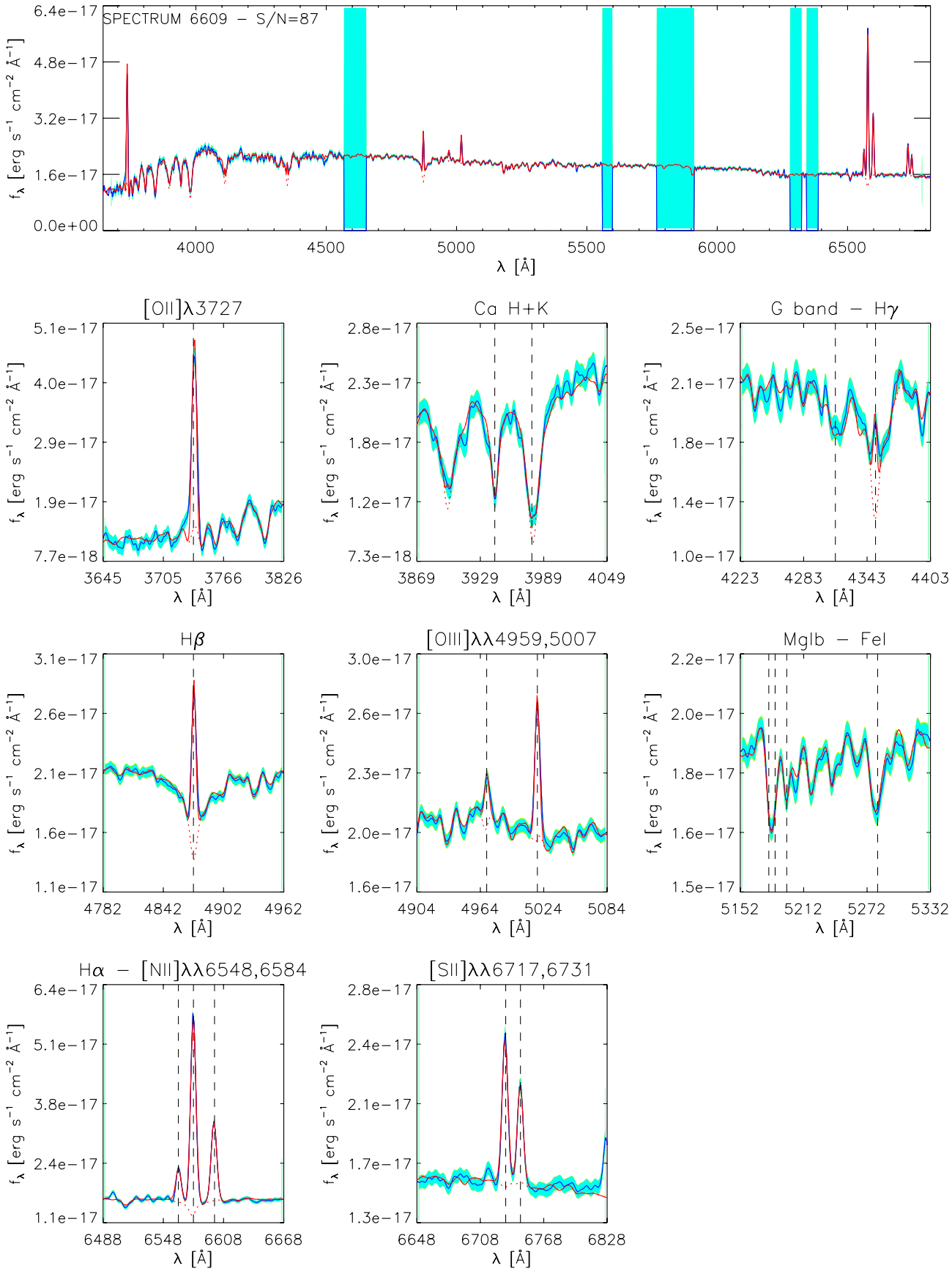

Figure 12. Observed and best-fit spectrum of a randomly selected spaxel in the NGC 628 data cube. The spectrum has an S/N of 87 in the continuum per spectral resolution element. The observed spectrum (solid blue) is shown with photometric errors (cyan envelope) and total errors (photometric plus systematic, green envelope). Also shown is the best-fit stellar plus emission line spectrum (solid red), and the best-fit stellar spectrum alone (dotted red). Vertical cyan bands represent regions masked around sky line residuals and the ends of the blue and red setup spectra. Also shown are zoomed-in relevant spectral features.

(A color version of this figure is available in the online journal.)

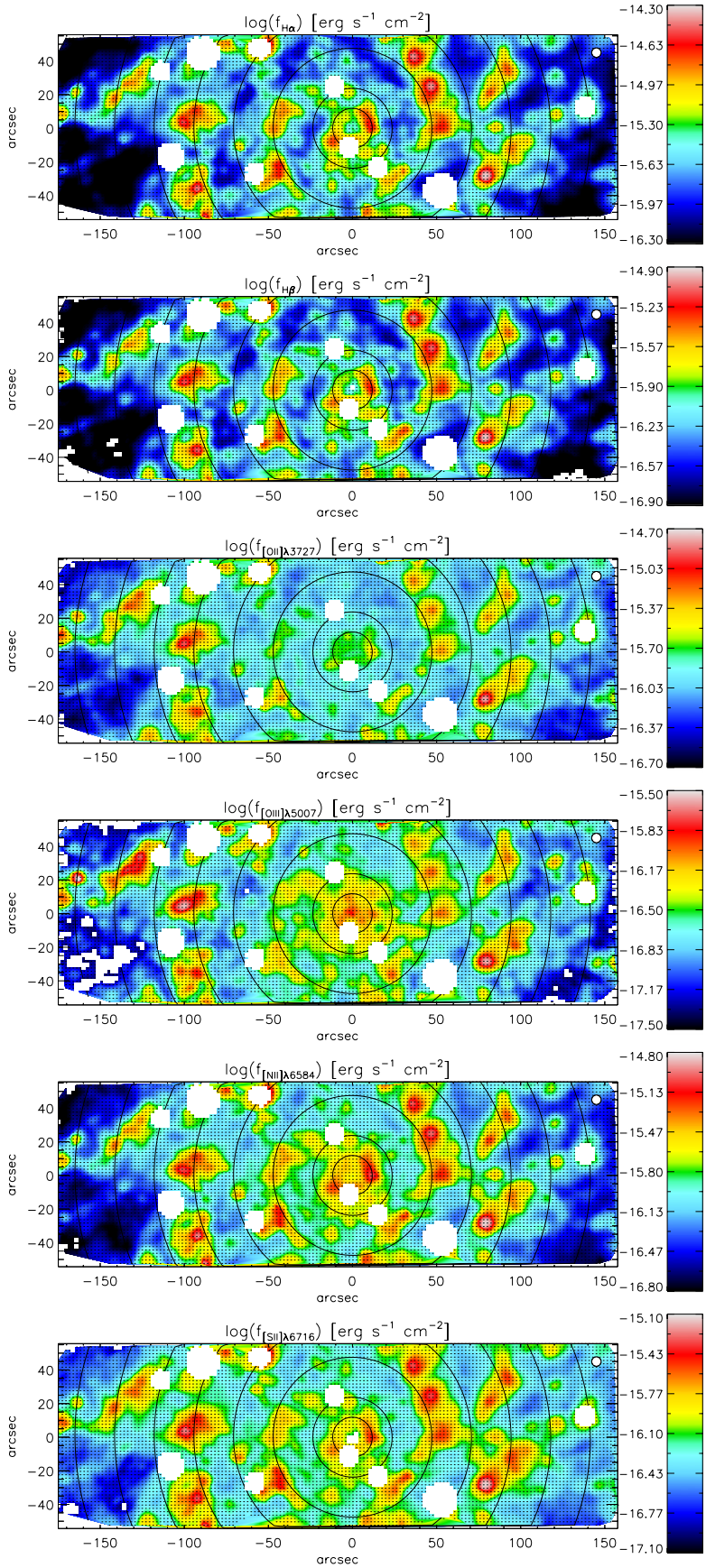

Figure 13. Maps of NGC 628 in different emission lines. From top to bottom: Hα, Hβ, [O II] λ3727, [O III] λ5007, [N II] λ6584, and [S II] λ6716. Black contours show lines of constant galactocentric radii spaced by 1 kpc, with the exception of the innermost contour at a radius of 0.5 kpc. Spaxels contaminated by foreground MW stars (see Section 6.1) are masked.

(A color version of this figure is available in the online journal.)

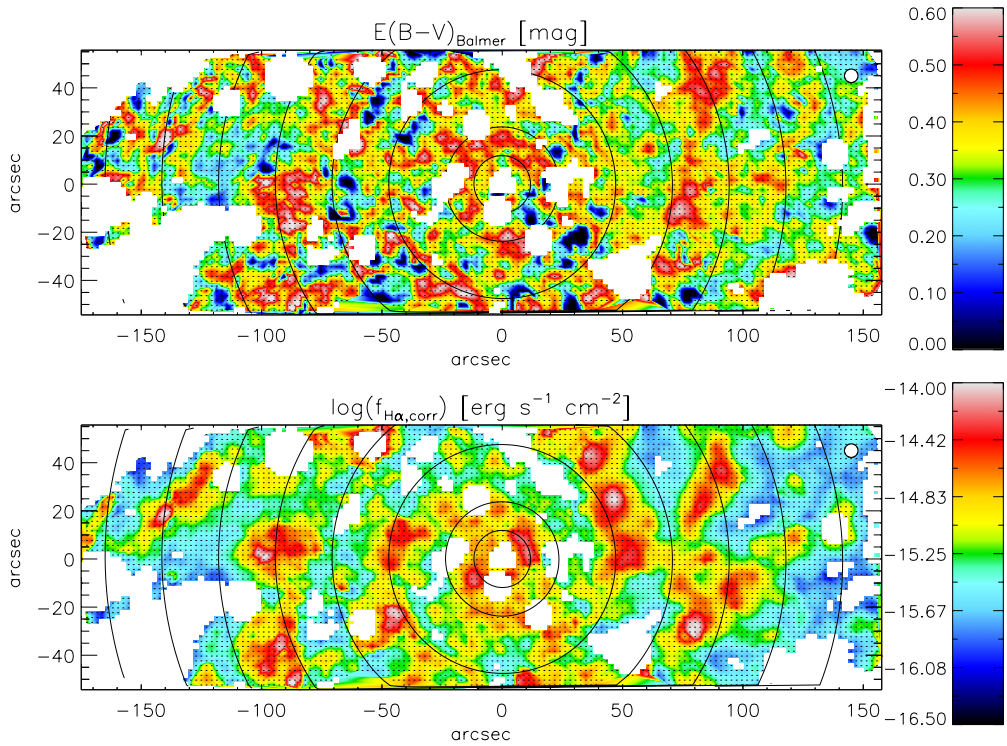

Figure 14. Upper panel: map of the dust reddening $E(B-V)$ computed using Equation (4). Regions where the uncertainty in $E(B-V)$ is larger than 0.2 mag have been masked. These masked regions correspond mainly to low-surface-brightness parts of the galaxy where the Hα to Hβ ratio cannot be measured with high S/N. Lower panel: map of the Hα emission line flux corrected for the effects of dust extinction using an MW extinction law. Black contours are as in Figure 13. Spaxels contaminated by foreground MW stars (see Section 6.1) are masked in both panels.

(A color version of this figure is available in the online journal.)

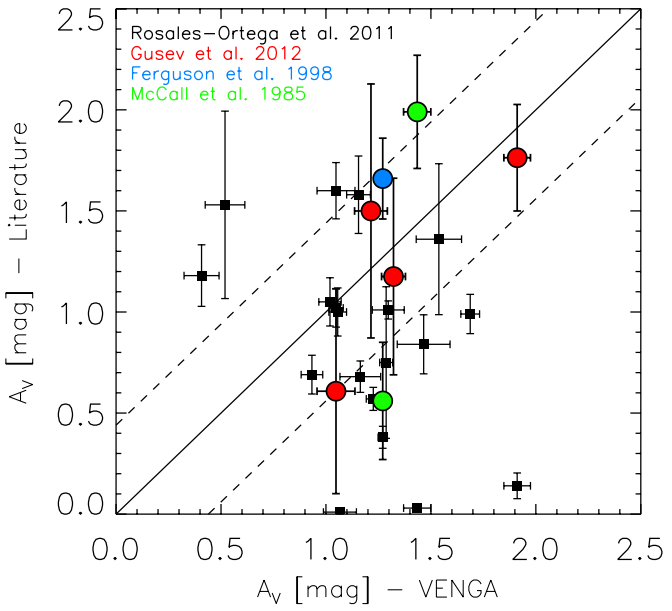

Figure 15. Comparison between the dust extinction (A_V) derived from the Balmer decrement in VENGA and measurements found in the literature for a sample of H II regions in the McCall et al. (1985), Ferguson et al. (1998), Rosales-Ortega et al. (2011), and Gusev et al. (2012) samples. Dashed lines indicate a 50% deviation in the dust correction.

(A color version of this figure is available in the online journal.)

In Figure 15 we compare the VENGA Balmer decrement dust extinction measurements to a compilation of H II region measurements in the literature. The VENGA data cube of NGC 628 covers 20 H II regions from the catalog of Rosales-Ortega et al. (2011; built from the PINGS IFU data cube of the galaxy), four H II regions from the multi-slit study of Gusev et al. (2012), and two H II regions from the McCall et al. (1985) sample, one of which was also studied by Ferguson et al. (1998). The two regions from the McCall et al. (1985) sample were also detected by PINGS, so the total number of unique comparison H II regions is 24. In our literature search we only considered regions with statistically significant extinction measurements in the respective studies.

Because of the large spatial resolution of our data, the comparison to seeing limited slit spectroscopy measurements is challenging. Even the PINGS data have a spatial resolution that is a factor of two smaller than ours. For the VENGA measurements we use the average extinction in a 5.″6 diameter aperture centered in each region, expecting the nebular emission in that spatial resolution element to be dominated by the H II region. Considering the differences in methodology, the comparison shows a reasonable agreement between the values measured in VENGA and those measured by previous authors. The observed scatter is consistent with the scatter seen in extinction among different studies. For the one H II region that is common to the Rosales-Ortega et al. (2011), McCall et al. (1985), and Ferguson et al. (1998) studies, the authors measure A_V values of 0.38, 0.56, and 1.66 mag, respectively, while the VENGA data yield an intermediate value of 1.27.

6. FITTING THE STELLAR AND IONIZED GAS VELOCITY FIELDS

In this section we present the methods used to fit the stellar and ionized gas velocity fields of NGC 628. We are interested in measuring the galaxy's rotation curve using both the stellar

and gaseous component with the goal of understanding any differences observed between both velocity fields. We propose a new method to measure the inclination of face-on disk galaxies, which is based on matching the gas and stellar rotation curves by means of the *asymmetric drift* correction.

6.1. Removal of Foreground Stars

In Figure 16 we present the stellar and ionized gas velocity field of NGC 628 resulting from the fits described in Section 5. Foreground MW stars can be clearly seen in the stellar velocity field as sources of low velocity along the line of sight. This is evident by looking at the SDSS *r*-band isophotes overplotted on the top panel of Figure 16. Guided by the SDSS broadband image, we flag these low-velocity spaxels in the data cube as spectra that are significantly contaminated by foreground stars. We mask all regions within 5″ of these flagged pixels. The resulting stellar and ionized gas velocity fields after the masking of foreground stars are shown in the second and bottom panels of Figure 16. Even at the low inclination of NGC 628 (see below for a discussion on the actual value) the VENGA data allow us to clearly detect the rotation of both the stellar and gaseous components of the galaxy.

6.2. Kinematic Position Angle and Systemic Velocity

We use the *symmetrization* method described in Appendix C of Krajnović et al. (2006) and implemented by Michele Cappellari in the IDL routine FIT_KINEMATIC_PA[17] to measure the kinematic position angle (P.A.) and systemic velocity ($v_{\rm sys}$) from both maps. In brief, for a given set of values (P.A., $v_{\rm sys}$), the method assumes mirror symmetry in the velocity field and a symmetrized velocity field is constructed by averaging the absolute values of the velocity at mirroring points on opposite sides of the perpendicular to the line of nodes. The best-fit P.A. and $v_{\rm sys}$ are those which minimize the residuals between the observed and symmetrized velocity fields.

For the kinematic P.A. we obtain consistent values of $20^\circ \pm 5^\circ$ and $22^\circ \pm 6^\circ$ for the stellar and ionized gas velocity fields, respectively. This value is in agreement with the RC3 *B*-band photometric P.A. of 25° (de Vaucouleurs et al. 1991), but is inconsistent with the 2MASS *K*-band reported value of 87.°5 (Jarrett et al. 2003). The kinematic P.A. of the ionized gas velocity field in the inner parts of the disk of NGC 628 has been measured independently in the past by Daigle et al. (2006) and Fathi et al. (2007) using Fabry–Perot Hα spectroscopy. These two studies measured inconsistent values of $26.^\circ4 \pm 2.^\circ4$ and $15^\circ \pm 5^\circ$. The value derived from the VENGA data sits right in between these two measurements and we consider it to be more reliable as it is based on deeper data, using the kinematics of multiple emission lines, and shows good agreement with the kinematic P.A. of the stellar component.

Kamphuis & Briggs (1992) used VLA H I 21 cm observations to reveal the presence of an extended H I disk in NGC 628, reaching out to a galactocentric radius of ∼30 kpc and showing complex morphology and kinematic structure. The H I velocity field shows a sharp transition in both P.A. and inclination around a galactocentric radius of 7′ (∼18 kpc), believed to be caused by the presence of a warp in the outer H I disk. The VENGA IFU data do not sample the disk out to such large galactocentric radii, but the stellar and ionized gas kinematics are consistent with the H I kinematics within the inner disk of the galaxy. The H I velocity field has a kinematic P.A. of ∼25° within the central 4′ (Figure 6 in Kamphuis & Briggs 1992), consistent with our measured value.

The symmetrization procedure also yields the systemic velocity of the galaxy. For the gaseous component we obtain a value of 650 ± 10 km s^{-1}, in agreement with the H I 21 cm derived values of 657 ± 1 km s^{-1} (Kamphuis & Briggs 1992) and 659 ± 3 km s^{-1} (Walter et al. 2008), but in stark disagreement with the value of 683 ± 3 km s^{-1} derived by Fathi et al. (2007) from the Hα velocity field. This inconsistency probably reflects a systematic error in the parameters of the kinematic model in Fathi et al. (2007), who also report a decreasing rotation curve within the central kiloparsec of the galaxy, a feature which is not observed either by Daigle et al. (2006) or in this study. The VENGA stellar velocity field yields a consistent systemic velocity of 651 ± 10 km s^{-1}, also agreement with the H I 21 cm derived values mentioned above.

6.3. Harmonic Decomposition Modeling

In order to measure the rotation curve of the galaxy we model the observed stellar and ionized gas velocity fields using the harmonic decomposition method (Franx et al. 1994; Wong et al. 2004; Krajnović et al. 2006). In particular, we use the IDL KINEMETRY[18] package to perform the fitting (Krajnović et al. 2006). We fit the azimuthal dependence of the LOS velocity along a set of elliptical annuli at different radii along the semimajor axis of NGC 628. The annuli semimajor axes are spaced following the combination of linear and logarithmic increase factors described in Krajnović et al. (2006) with a minimum radius of 6″. For each ellipse the LOS velocity is fitted as

$$v(R, \psi) = v_{\rm sys} + \sum_{n=1}^{3} [A_n(R)\sin(n\psi) + B_n(R)\cos(n\psi)], \quad (5)$$

where $v_{\rm sys}$ is the systemic velocity measured independently for each component in the previous section, R is the ellipse semimajor axis, and ψ is the eccentric anomaly angle. The outermost radius at which the fit is performed is set by the requirement that data are available for 70% of the points along the ellipse. For NGC 628, this translates to an outermost radius of 60″ (≃2.5 kpc).

During the fitting, the geometric parameters of the ellipses (center, P.A., and inclination) are held fixed. We use the average of the two globally derived kinematic P.A.s for stars and gas of 21° (Section 6.2), and the central coordinates from NED.[19] As discussed below, the choice of an inclination value for NGC 628 is far from trivial.

Using photometric axis ratios ($q = b/a$) to compute the inclination of NGC 628 by adopting the Tully (1988) method, we derive $i = 28^\circ$ ($q = 0.91$) for the RC3 *B*-band measurements (de Vaucouleurs et al. 1991) and $i = 34^\circ$ ($q = 0.86$) for the 2MASS *K*-band photometry (Jarrett et al. 2003). The detailed photometric decomposition of Fisher & Drory (2008) implies an inclination of $i = 33^\circ$ ($q = 0.87$) for the disk component. Given the projected circular velocities measured at large radii in both the 21 cm H I and Hα velocity fields (Kamphuis & Briggs 1992; Daigle et al. 2006; Fathi et al. 2007), such inclinations would imply a deprojected velocity of $v_{\rm flat} \sim 50$ km s^{-1} for

[17] http://www-astro.physics.ox.ac.uk/~mxc/idl/

[18] http://www.eso.org/dkrajnov/idl/#kinemetry

[19] The NASA/IPAC Extragalactic Database (NED) is operated by the Jet Propulsion Laboratory, California Institute of Technology, under contract with the National Aeronautics and Space Administration.

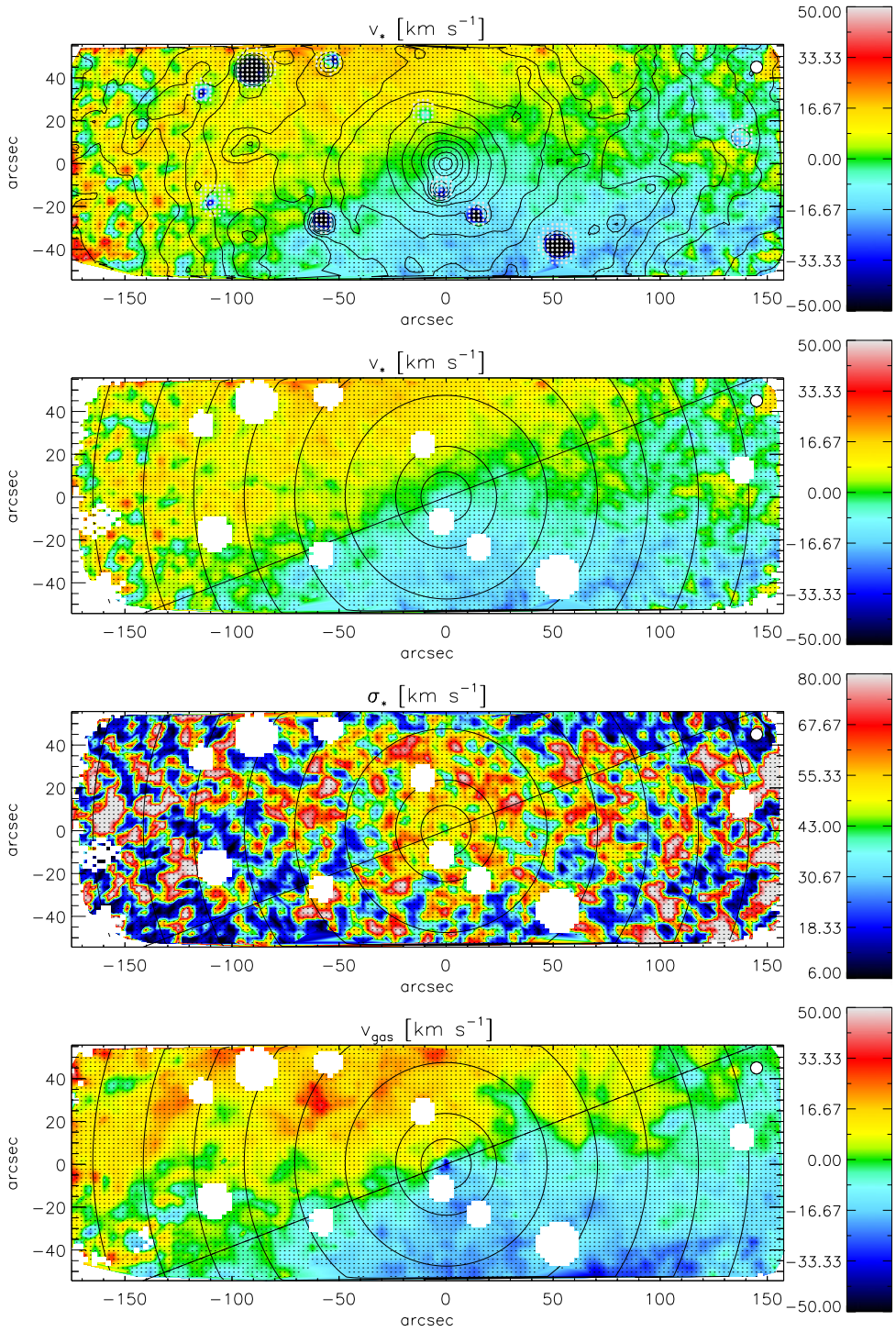

Figure 16. First panel: map of the stellar LOS velocity (v_*) in NGC 628. Black contours mark SDSS *r*-band isophotes as in Figure 9. Gray dots mark spaxels flagged as contaminated by foreground stars. Second panel: clean map of the stellar LOS velocity where both foreground stars and regions with an error in v_* larger than 15 km s^{-1} have been masked. Third panel: map of the LOS stellar velocity dispersion ($\sigma_* = \sigma_{\rm LOS}$) measured from the fit to the Mg I *b* region. Lower panel: map of the ionized gas LOS velocity ($v_{\rm gas}$) as measured from the simultaneous fit to all emission lines listed in Table 6. Regions having an error in $v_{\rm gas}$ larger than 15 km s^{-1} have been masked. The zero-velocity line for the measured 21° P.A. is marked by the diagonal solid black line in the bottom three panels.

(A color version of this figure is available in the online journal.)

the flat part of the rotation curve. Such a small circular velocity is wildly inconsistent with expectations from the Tully–Fisher (TF) relation (Tully & Fisher 1977) for NGC 628.

Using the *K*-band TF relation from Verheijen (2001)[20] and the 2MASS *K*-band absolute magnitude from Table 1 we obtain $v_{\rm flat,TF} = 149 \pm 3 \pm 8$ km s^{-1}, where the random error comes from the uncertainty in the distance and apparent magnitude of the galaxy and the systematic uncertainty comes from the 0.26 mag scatter in the adopted TF relation. The inconsistency between this value and that derived from the photometrically measured inclination is not surprising given that the uncertainty in *i* explodes as one approaches a nearly face-on configuration.

[20] We use the parameters from the fit to their "RC/FD Sample, Excluding NGC 3992" in Table 4 of Verheijen (2001).

This is also the case for kinematically derived inclinations. In fact, letting the inclination be a free parameter for the ellipses in our harmonic decomposition fits yields an unrealistic median value of $i = 45°$. Daigle et al. (2006) derive a kinematic inclination of $21.^{\circ}5 \pm 4.^{\circ}5$ from their tilted ring analysis of the Hα velocity field. For an excellent discussion on the uncertainties associated with measuring the inclination of disk galaxies, see Bershady et al. (2010b).

Given the unreliability of both photometric and kinematic inclinations for face-on galaxies, most studies of NGC 628 have assumed a value of $i = 6.^{\circ}5$ (e.g., Kamphuis & Briggs 1992; Daigle et al. 2006; Fathi et al. 2007; Herbert-Fort et al. 2010). This value was adopted by Kamphuis & Briggs (1992) so the flat part of the H I rotation curve would reach an arbitrary chosen value of $v_{\rm flat} = 200$ km s^{-1}. A notable exception is the work of Herrmann & Ciardullo (2009), who fit an exponential model to the THINGS 21 cm H I velocity field of NGC 628 to obtain an inclination of $i = 9°$.

Under the assumption that NGC 628 exactly follows the TF relation, a better value for the inclination would be $i_{\rm TF} = 8.^{\circ}7 \pm 0.^{\circ}7$ (assuming an error of 10 km s^{-1} for the value of $v_{\rm flat}$ measured at large radii by Kamphuis & Briggs (1992) and propagating the errors in the apparent magnitude and distance of NGC 628 as well as the scatter in the TF relation). This so-called "Tully–Fisher inclination" method is discussed in Bershady et al. (2010b) and provides more reliable estimates of the inclination for face-on systems than photometric or kinematic techniques.

In the following section we propose a new alternative method to derive the inclination of face-on disk galaxies by demanding agreement between the ionized gas and stellar rotation curves after applying the asymmetric drift correction to the stellar component.

6.4. Rotation Curve and Asymmetric Drift Correction: A New Method to Measure Inclinations

Because of the collisional nature of gas, as opposed to the collisionless nature of stars, the cold ISM of disk galaxies is expected to be confined to a relatively thin disk supported mainly by rotation. Although pressure support in the ISM can become important under certain circumstances (e.g., high turbulence, strong pressure gradients, etc.), the small and relatively constant Hα velocity dispersion of $\sigma_{\rm H\alpha} \sim 17$ km s^{-1} measured by Fathi et al. (2007) across the disk of NGC 628 implies that the gaseous disk of this galaxy is almost fully supported by circular motions, with random motions only having a minor effect. The importance of pressure support against gravity in gaseous galactic disks is extensively discussed in Dalcanton & Stilp (2010). Using the flat dispersion profile of Fathi et al. (2007) and applying Equation (11) from Dalcanton & Stilp (2010), we compute a correction to the ionized gas rotation curve of NGC 628 of $\sim$2 km s^1. This is many times smaller than the 1σ uncertainty in the rotation curve itself. Given the small magnitude of this effect we decide not to apply these corrections and neglect the effect of pressure support in the gaseous disk of NGC 628. Therefore we consider the ionized gas rotation curve to roughly follow the dynamics of a test particle under the gravitational potential in the midplane of the galaxy.

Stellar disks can also experience support against gravity provided by random motions. As in the case of pressure support in gaseous disks, stellar random motion support translates into a measured circular velocity that is smaller than the actual circular velocity at which a test particle would orbit in the gravitational potential of the galaxy. This effect, first noted as a difference in orbital velocity for stellar populations of different ages (and therefore different velocity dispersions) in the solar neighborhood, is known as "asymmetric drift" (Stromberg 1922). As noted by Dalcanton & Stilp (2010) the equations describing it are similar to those describing pressure support in gaseous disks, but the physical phenomena are fundamentally different.

Starting from the Jeans equations (Jeans 1915) and following Binney & Tremaine (1987), for a stellar axisymmetric disk in steady state, under the assumption that the "epicyclic approximation" holds and that the stellar velocity ellipsoid (SVE) is aligned with the disk in cylindrical coordinates and its shape is independent of the vertical distance to the plane, the quadratic difference between the true and the observed circular velocities is given by

$$v_c^2 - v_\phi^2 = \frac{\sigma_R^2}{2}\left(\frac{\partial \ln(v_\phi)}{\partial \ln(R)} - 1 - 2\frac{\partial \ln(\nu\sigma_R^2)}{\partial \ln(R)}\right), \qquad (6)$$

where v_c is the circular velocity of a test particle in the potential, v_ϕ is the observed circular velocity, σ_R is the velocity dispersion in the radial direction, and ν is the number density of stars. While v_ϕ and its logarithmic derivative with radius can be directly measured from the harmonic decomposition fits described in Section 6.3, calculating the last term in parentheses in Equation (6) requires making a series of assumptions that we describe below.

In order to apply the asymmetric drift correction we assume a constant scale height and V-band mass-to-light ratio for the disk of NGC 628. These assumptions imply that $\nu(R)$ is proportional to the stellar mass surface density $\Sigma(R)$ and that the latter is well traced by the surface brightness profile of the galaxy. In particular, we use the best-fit disk-plus-pseudo-bulge V-band decomposition of Fisher & Drory (2008) to trace the radial dependence of $\nu(R)$ when calculating the last term in Equation (6). Note that knowledge of the V-band mass-to-light ratio is not necessary as it cancels out in the logarithmic derivative.

Using a measurement of the stellar velocity dispersion along the line of sight ($\sigma_{\rm LOS}(R)$), we can estimate $\sigma_R(R)$, given our assumptions regarding the shape and orientation of the SVE. The third panel in Figure 16 presents the map of the stellar velocity dispersion ($\sigma_* = \sigma_{\rm LOS}$) measured from the VENGA data in Section 5.1. In the central regions of NGC 628 we see σ_* falling from a central value of $\sim$60 km s^{-1}. Figure 17 presents the radial profile of $\sigma_{\rm LOS}$. To measure the radial profile we only considered spaxels with high enough S/N as to provide a reliable fit of the LOSVD (i.e., those which are not masked in Figure 16). Red circles mark the median $\sigma_{\rm LOS}$ in 0.5 kpc wide radial bins. Error bars show both the standard deviation in each radial bin (red) and the median error in σ_* for each spaxel (black).

Also plotted in Figure 17 is the central stellar velocity dispersion value of $\sigma_*(R = 0) = 72.2 \pm 7.8$ km s^{-1} from HyperLeda[21] (blue circle). The HyperLeda value is an average over six literature measurements and is driven by an outlier at 116 km s^{-1} (di Nella et al. 1995). Rejecting this outlier, the HyperLeda average comes down to 64 km s^{-1}, in even better agreement with our measurements (blue triangle in Figure 17). The velocity dispersions we measure in the central regions of the galaxy are also consistent with the nuclear value of

[21] http://leda.univ-lyon1.fr/

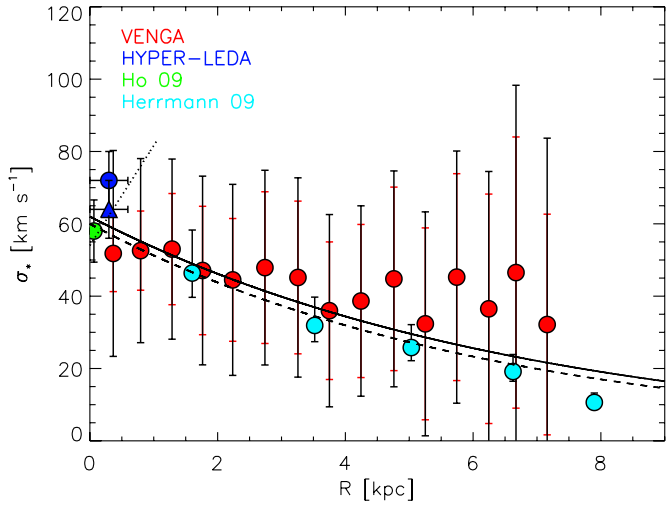

Figure 17. Radial profile of $\sigma_* = \sigma_{\rm LOS}$. Red circles mark the median σ_* for all spaxels in 0.5 kpc wide radial bins. Error bars show both the standard deviation in each radial bin (red) and the median error in σ_* for each spaxel (black). The central stellar velocity dispersion values from HyperLeda and Ho et al. (2009) are shown in blue and green, respectively. The dispersion profile measured by Ganda et al. (2006) using the SAURON IFU spectroscopy is shown as a black dashed curve. The velocity dispersion profile measured from PN kinematics by Herrmann & Ciardullo (2009) is also shown (light blue circles, dashed line). The solid black curve shows the best-fit dispersion profile to the VENGA data used to calculate the asymmetric drift correction.

(A color version of this figure is available in the online journal.)

58.0 ± 8.6 km s^{-1} measured by Ho et al. (2009; green circle). Our measurements also agree with the central dispersion of 54 ± 10 km s^{-1} measured by Ganda et al. (2006) using SAURON IFU spectroscopy. The radial σ_* profile measured in this last study is shown as a dashed black line in Figure 17. While our measured values in the center of the galaxy are consistent with the ones in Ganda et al. (2006), we find no evidence to support their claim of an increasing velocity dispersion with radius in NGC 628. At larger radii Figure 17 shows the dispersion profile measured by Herrmann & Ciardullo (2009) using the kinematics of a large sample of planetary nebulae (PNs). The dashed line shows the best-fit dispersion profile from Herrmann & Ciardullo (2009), which follows an exponential with a scale length approximately equal to two times the photometric scale length of the galaxy. The latter agrees with theoretical expectations for constant scale height disks in which $\sigma_z(R) \propto \sqrt{\Sigma_{\rm disk}(R)}$, with the proportionality constant depending on the detailed vertical profile of the disk (exponential, sech or sech^2, van der Kruit 1988; Bershady et al. 2010a; van der Kruit & Freeman 2011 and references therein).

The 145 km s^{-1} spectral resolution at Mg I b in the VENGA VIRUS-P data makes the measurement of such low values of the velocity dispersions very challenging. The large error bars in Figure 17 indicate that for single spectra, individual measurements of low dispersion values ($\sim$50 km s^{-1}) are extremely noisy even at the high S/N $\sim$ 100 of our data. Nevertheless, by averaging over many spaxels in the data cube we seem to recover the velocity dispersion profile of the galaxy at least out to $R \simeq 4$ kpc where the VENGA measurements flatten around a value of $\sim$40 km s^{-1}. Comparison to the dispersion profile derived from PN kinematics shows that this flattening is not real and most likely corresponds to a systematic floor caused by uncertainties associated with template mismatch and deviations from the assumed Gaussianity in the instrumental line spread function most likely set this limit. This is not surprising given that it happens at about a fourth of the instrumental resolution and that a similar behavior is seen in the simulations presented in Section 5.2.

We fit an exponential dispersion profile to the VENGA data in the 1.5 kpc $< R <$ 4 kpc region in order to avoid regions in which the stellar dynamics are contaminated by the central spheroidal component (see discussion in Bershady et al. 2010b). We fix the scale length of the profile to two times the scale length of the disk component in the Fisher & Drory (2008) decomposition. The best-fit profile is shown as a solid line in Figure 17, implies a central velocity dispersion of $\sigma_{\rm LOS}(0) = 62$ km s^{-1} (consistent with the HyperLeda, Ho et al. 2009 and Ganda et al. 2006 values), and is in excellent agreement with the Herrmann & Ciardullo (2009) best-fit profile and with theoretical expectations for the dynamics of stellar disks. This $\sigma_{\rm LOS}(R)$ profile is used to derive $\sigma_{\rm R}(R)$ in order to calculate the asymmetric drift correction using Equation (6).

Following the method outlined in Bershady et al. (2010b) we assume the following shape for the SVE in order to deproject the LOS velocity dispersion profile and compute $\sigma_R(R)$:

$$\alpha = \frac{\sigma_z}{\sigma_R} = 0.6 \tag{7}$$

$$\beta = \frac{\sigma_\phi}{\sigma_R} = \sqrt{\frac{1}{2}\left(\frac{\partial \ln(v_\phi)}{\partial \ln(R)} + 1\right)}, \tag{8}$$

where the first equation comes from expectations from the solar neighborhood (Binney & Merrifield 1998) and observations of nearby galaxies (Bershady et al. 2010b) and the second comes from adopting the epicyclic approximation. This allows us to compute all the terms in Equation (6) and apply the asymmetric drift correction to the stellar velocity field of the galaxy. We use Monte Carlo simulations to calculate the error in the asymmetric drift correction. In the error calculation we include the uncertainty in the observed rotation curve, which is propagated to compute the uncertainty in the logarithmic radial derivative of the rotation curve and the value of β, an error of $\Delta\alpha = 0.15$ (Bershady et al. 2010b), and an error in $\sigma_{\rm LOS}(0)$ of 10 km s^{-1}.

In the upper panel of Figure 18 we present the VENGA rotation curve of NGC 628 for both stars (black circles) and ionized gas (red circles), as measured from the first-order cosine term of the harmonic decomposition model $v_{\rm circ}(R) = B_1(R)/\sin(i)$. We show measurements of the rotation curve for two different assumed inclination values of $i = 28°$ (derived from the RC3 axis ratios, open circles) and $i = 6\overset{\circ}{.}5$ (Kamphuis & Briggs 1992, filled circles). The horizontal dashed line marks the expectation from the TF relation $v_{\rm flat,TF} = 149$ km s^{-1} (Section 6.3). The high inclination implied by the photometric axis ratio dramatically underestimates the amount of rotation expected in NGC 628. This highlights the lack of reliability of geometrically measured inclinations in face-on systems.

Independent of the assumed inclination, the observed stellar circular velocity (before applying the asymmetric drift correction) is systematically lower than the observed circular velocity of the gaseous component. This implies the presence of significant kinematic support arising from random motions in the stellar disk of NGC 628. For the $i = 6\overset{\circ}{.}5$ case the corrected stellar rotation curve after accounting for asymmetric drift using Equation (6) is shown by the black open squares in the top panel of Figure 18. Error bars in the corrected stellar rotation curve are calculated using Monte Carlo simulations and including the

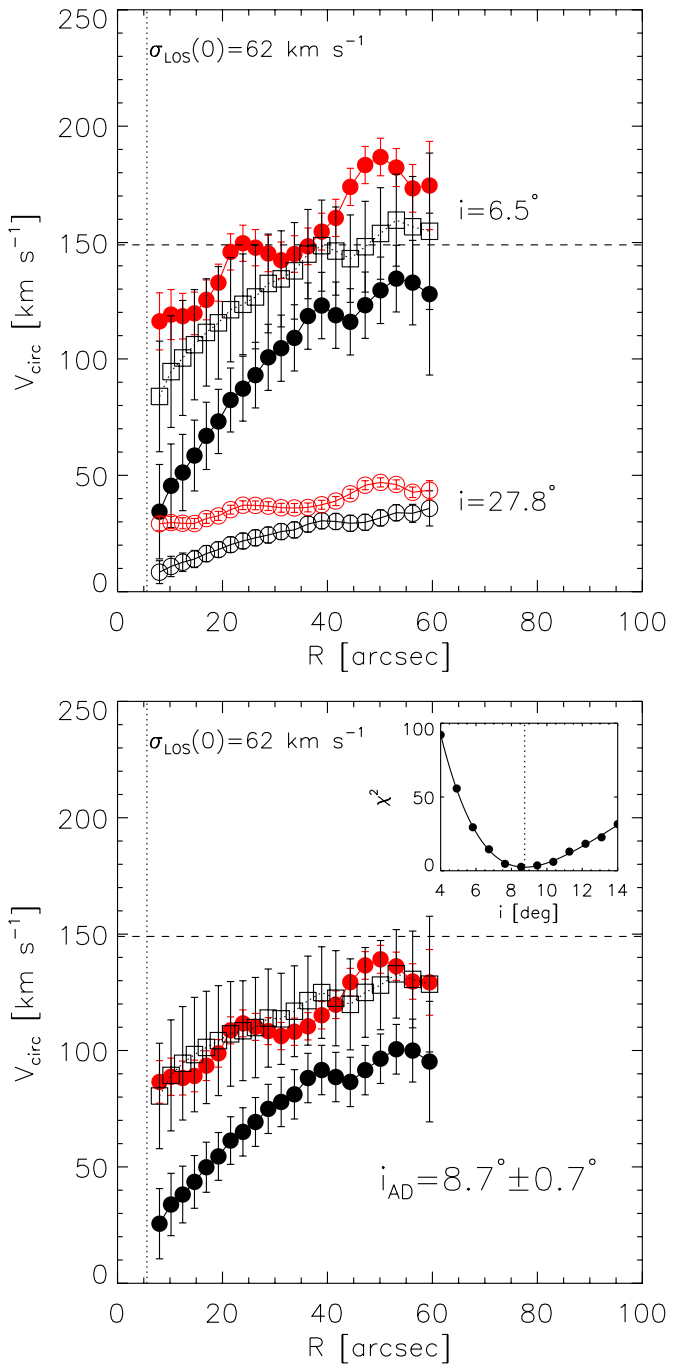

Figure 18. Top panel: stellar (black) and ionized gas (red) rotation curves for NGC 628 under the assumption of two different inclination values of 6.°5 (filled circles) and 27.°8 (open circles). Open squares show the stellar rotation curve after applying the asymmetric drift correction for the $i = 6.°5$ case. The horizontal dashed line marks the asymptotic rotation velocity of 149 km s^{-1} expected from the Tully–Fisher relation. The size of the VENGA PSF FWHM is marked by the dotted vertical line. Lower panel: same as above, but for the best-fit *asymmetric drift inclination* ($i_{AD} = 8.°7 \pm 0.°7$). The inset shows the χ^2 distribution for the range of inclination values explored during the fit. The vertical dotted line in the inset marks the best-fit inclination.

(A color version of this figure is available in the online journal.)

uncertainty in all the quantities entering the correction. For an assumed value of $i = 6.°5$, the magnitude of the asymmetric drift correction is not sufficient to account for the discrepancy between the observed stellar and gaseous rotation curves.

The above problem can be solved by changing the assumed value for the inclination. We remind the reader that the $i = 6.°5$ value typically used in the literature for NGC 628 was arbitrarily adopted by Kamphuis & Briggs (1992) to make the flat part of the rotation curve reach a velocity of 200 km s^{-1}. From the TF relation we have seen in Section 6.3 that the expected asymptotic velocity in the flat part of the rotation curve of NGC 628 is smaller than what was assumed by Kamphuis & Briggs (1992) with a value closer to 150 km s^{-1}. This asymptotic velocity implies an inclination of $i_{TF} = 8.°7$.

The lower panel in Figure 18 shows the result of matching the gas and asymmetric drift corrected stellar rotation curves to obtain the inclination i_{AD} of the galaxy. The method consists of sampling a range of inclination values in order to find the inclination that minimizes the residuals between both rotation curves. For each inclination value we measure the rotation curves by performing harmonic decomposition fits to the velocity fields, we deproject the LOS velocity dispersion profile to compute the asymmetric drift correction, and we compute a χ^2 statistic in order to quantify deviations between the gas and corrected stellar rotation curves.

The inset in the lower panel of Figure 18 shows the χ^2 distribution as a function of inclination. The minimum χ^2 corresponds to a best-fit value for the *asymmetric drift inclination* of $i_{AD} = 8.°7 \pm 0.°7$ in perfect agreement with the $i_{TF} = 8.°7 \pm 0.°7$ value derived from the TF relation. The exact agreement in both the value and the error bars implies that both methods produce consistent results with similar precisions, at least in the case of NGC 628. The TF and asymmetric drift methods are highly complementary. The TF method requires knowledge of the observed rotation velocity in the flat part of the rotation curve at large radii, while the asymmetric drift method can be used even when only kinematic measurements are only available in the central regions of galaxies. Furthermore, the measurement of independent *asymmetric drift inclinations* can allow for highly inclined systems to be included when measuring the TF relation.

We propose the matching of the gaseous and asymmetric-drift-corrected stellar rotation curves as a new method to estimate the inclination of nearly face-on disk galaxies. The fact that a very small difference of 2.°2 in the adopted inclination can produce a catastrophic inconsistency between the observed gas and stellar kinematics as in the $i = 6.°5$ case highlights the sensitivity of this method as a tool to measure inclinations.

7. SUMMARY AND CONCLUSIONS

In this work we have presented the survey design, sample, observing strategy, data reduction, and spectral analysis methods for VENGA. Wide-field integral field spectroscopy proves to be a powerful tool to study a large set of physical phenomena occurring in nearby galaxies. We characterized our sample of 30 nearby disk galaxies in terms of their stellar masses and SFRs, and showed that VENGA is a representative sample of massive ($>10^{10}\ M_\odot$) spiral galaxies in the local universe. A large range of morphological parameters (bulge-to-disk ratio, bar presence, bulge Sérsic index, inclination) is represented in the sample. The distance distribution of our targets implies a median spatial resolution in physical units of 383 pc. Our targets typically span a few arcminutes in angular size, and we tile the VIRUS-P IFU in order to provide a coverage out to 0.7 R_{25} for most galaxies. This implies that the VENGA data cubes are among the largest optical IFU data cubes ever constructed. In particular, the NGC 628 data cube presented in this paper spans $5.'2 \times 1.'7$.

The wealth of information produced by integral field spectrographs stresses the need for optimized and pipelined software tools to process and analyze the data. This becomes essential

when this observational technique is used to conduct large surveys like the one presented here. We have presented the reduction and calibration pipeline used for the VENGA data. We have also described our spectral analysis pipeline, which we use to extract stellar and gas kinematics as well as emission line fluxes, and we have discussed the methods used to estimate the uncertainties in all these parameters. When possible, we have adapted existing publicly available software to be used on the VIRUS-P data. We assessed the quality of the VENGA data obtained on NGC 628 and we find it to be excellent. VIRUS-P provides high S/N spectra for single fibers out to large galactocentric radii. Thanks to the ability of reconstructing broadband images from the IFU data and cross-correlating them with archival broadband images of the galaxies in our sample, we can achieve good astrometric precision ($\sim 0\farcs1$) and better than 10% flux calibration accuracy across the full wavelength range.

Finally, we have used a harmonic decomposition technique to fit the stellar and ionized gas velocity fields in NGC 628. The observed kinematics imply that the gaseous disk of the galaxy (as traced by nebular emission from ionized gas) is almost fully supported by rotation while the stellar disk shows significant levels of dynamic support arising from random motions. This is evident by a $\sim$50 km s^{-1} offset between the ionized gas and stellar rotation curves.

We have shown that the above discrepancy in the rotation curves can be explained if one takes into account the effect of stellar random motions by applying an asymmetric drift correction. The agreement between the ionized gas rotation curve and the asymmetric drift corrected stellar rotation curve depends strongly on the assumed value for the inclination. We take advantage of this dependence and propose this as a method to estimate the actual inclination of nearly face-on disk galaxies for which classically used geometrically derived inclinations are extremely unreliable. Applying this method, we find a revised asymmetric drift inclination for NGC 628 of $i_{\rm AD} = 8\fdg7 \pm 0\fdg7$, in excellent agreement with the expected value of $i = 8\fdg7 \pm 0\fdg7$, which comes from assuming that NGC 628 satisfies the local TF relation.

The main purpose of this work is to present the VENGA survey and some preliminary scientific results have been discussed only briefly. We expect to use the VENGA sample to conduct a series of studies on star formation, galactic structure assembly, stellar populations, chemical evolution, galactic feedback, nuclear activity, and the properties of the ISM in massive disk galaxies, and to present these results in a series of future publications. As an example of the practical uses of these data, in a recent paper we have presented a study of the radial profile in the CO-to-H_2 conversion factor $X_{\rm CO}$ and its relation to other parameters like the metallicity, the gas surface density, and the ionization parameter across the disk of NGC 628 (Blanc et al. 2013).

Once all of the VENGA data are processed we expect to make it publicly available to the community. The richness of large IFU data sets like the one we are compiling goes beyond the scientific goals of our team. We expect VENGA to be a useful resource that will complement the wealth of multi-wavelength data sets that the community has acquired on nearby spiral galaxies over the last few decades.

The VENGA collaboration acknowledges the generous support from the Norman Hackerman Advanced Research Program (NHARP) ARP-03658-0234-2009. G.A.B. acknowledges the support of Sigma Xi, The Scientific Research Society, Grant in Aid of Research. N.J.E. and A.L.H. were supported by NSF Grant AST-1109116. R.X.L. and L.H. acknowledge the support by the National Natural Science Foundation of China under grant No. 11073040, by the 973 Program of China under grant No. 2009CB824800, and by the Shanghai Pujiang Talents Program under grant No. 10pj1411800. The construction of the Mitchell Spectrograph (formerly VIRUS-P) was possible thanks to the generous support of the Cynthia & George Mitchell Foundation. We thank Phillip McQueen and Gary Hill for designing and constructing VIRUS-P, and for their advice on the use of the instrument. We also acknowledge David Doss and the staff at McDonald Observatory for their invaluable help during the observations. This research has made use of NASA's Astrophysics Data System, and of the NASA/IPAC Extragalactic Database (NED), which is operated by the Jet Propulsion Laboratory, California Institute of Technology, under contract with the National Aeronautics and Space Administration.

REFERENCES

Adams, J. J., Blanc, G. A., Hill, G. J., et al. 2011, ApJS, 192, 5
Adams, J. J., Gebhardt, K., Blanc, G. A., et al. 2012, ApJ, 745, 92
Bacon, R., Copin, Y., Monnet, G., et al. 2001, MNRAS, 326, 23
Beifiori, A., Maraston, C., Thomas, D., & Johansson, J. 2011, A&A, 531, A109
Bernardi, M., Sheth, R. K., Annis, J., et al. 2003, AJ, 125, 1817
Bershady, M. A., Andersen, D. R., Harker, J., Ramsey, L. W., & Verheijen, M. A. W. 2004, PASP, 116, 565
Bershady, M. A., Verheijen, M. A. W., Swaters, R. A., et al. 2010a, ApJ, 716, 198
Bershady, M. A., Verheijen, M. A. W., Westfall, K. B., et al. 2010b, ApJ, 716, 234
Binney, J., & Merrifield, M. (ed.) 1998, Galactic Astronomy (Princeton Series in Astrophysics; Princeton, NJ: Princeton Univ. Press)
Binney, J., & Tremaine, S. 1987, Galactic Dynamics (Princeton, NJ: Princeton Univ. Press)
Blanc, G. A., Heiderman, A., Gebhardt, K., Evans, N. J., II, & Adams, J. 2009, ApJ, 704, 842
Blanc, G. A., Schruba, A., Evans, N. J., II, et al. 2013, ApJ, 764, 117
Blumenthal, G. R., Faber, S. M., Primack, J. R., & Rees, M. J. 1984, Natur, 311, 517
Brinchmann, J., Charlot, S., White, S. D. M., et al. 2004, MNRAS, 351, 1151
Cappellari, M., & Emsellem, E. 2004, PASP, 116, 138
Cappellari, M., Emsellem, E., Krajnović, D., et al. 2011, MNRAS, 413, 813
Cortés, J. R., Kenney, J. D. P., & Hardy, E. 2008, ApJ, 683, 78
Croton, D. J., Springel, V., White, S. D. M., et al. 2006, MNRAS, 365, 11
Daigle, O., Carignan, C., Amram, P., et al. 2006, MNRAS, 367, 469
Dalcanton, J. J., & Stilp, A. M. 2010, ApJ, 721, 547
Davé, R., Finlator, K., & Oppenheimer, B. D. 2011, MNRAS, 416, 1354
de Jong, R. S. 1996, A&A, 313, 377
Dekel, A., Birnboim, Y., Engel, G., et al. 2009, Natur, 457, 451
de Vaucouleurs, G., de Vaucouleurs, A., Corwin, H. G., Jr.,, et al. (ed.) 1991, Third Reference Catalogue of Bright Galaxies. Volume I: Explanations and References. Volume II: Data for Galaxies between 0^h and 12^h, Volume III: Data for Galaxies between 12^h and 24^h (New York: Springer), 2091
de Zeeuw, P. T., Bureau, M., Emsellem, E., et al. 2002, MNRAS, 329, 513
di Nella, H., Garcia, A. M., Garnier, R., & Paturel, G. 1995, A&AS, 113, 151
Dong, X. Y., & De Robertis, M. M. 2006, AJ, 131, 1236
Dunkley, J., Komatsu, E., Nolta, M. R., et al. 2009, ApJS, 180, 306
Fabricius, M. H., Barnes, S., Bender, R., et al. 2008, Proc. SPIE, 7014, 701473
Falcón-Barroso, J., Sánchez-Blázquez, P., Vazdekis, A., et al. 2011, A&A, 532, A95
Fathi, K., Beckman, J. E., Zurita, A., et al. 2007, A&A, 466, 905
Ferguson, A. M. N., Gallagher, J. S., & Wyse, R. F. G. 1998, AJ, 116, 673
Fisher, D. B., & Drory, N. 2008, AJ, 136, 773
Förster Schreiber, N. M., Genzel, R., Lehnert, M. D., et al. 2006, ApJ, 645, 1062
Franx, M., van Gorkom, J. H., & de Zeeuw, T. 1994, ApJ, 436, 642
Freedman, W. L., Madore, B. F., Gibson, B. K., et al. 2001, ApJ, 553, 47
Fumagalli, M., Prochaska, J. X., Kasen, D., et al. 2011, MNRAS, 418, 1796
Ganda, K., Falcón-Barroso, J., Peletier, R. F., et al. 2006, MNRAS, 367, 46
Genzel, R., Tacconi, L. J., Eisenhauer, F., et al. 2006, Natur, 442, 786
Greene, J. E., & Ho, L. C. 2006, ApJ, 641, 117

Gusev, A. S., Pilyugin, L. S., Sakhibov, F., et al. 2012, MNRAS, 424, 1930
Haffner, L. M., Dettmar, R.-J., Beckman, J. E., et al. 2009, RvMP, 81, 969
Heiderman, A. L. 2012, American Astronomical Society Meeting Abstracts, 219, 208.03
Herbert-Fort, S., Zaritsky, D., Christlein, D., & Kannappan, S. J. 2010, ApJ, 715, 902
Herrmann, K. A., & Ciardullo, R. 2009, ApJ, 705, 1686
Herrmann, K. A., Ciardullo, R., Feldmeier, J. J., & Vinciguerra, M. 2008, ApJ, 683, 630
Hill, G. J., MacQueen, P. J., Smith, M. P., et al. 2008, Proc. SPIE, 7014, 231
Ho, L. C. 2008, ARA&A, 46, 475
Ho, L. C., Greene, J. E., Filippenko, A. V., & Sargent, W. L. W. 2009, ApJS, 183, 1
Jacobs, B. A., Rizzi, L., Tully, R. B., et al. 2009, AJ, 138, 332
Jarrett, T. H., Chester, T., Cutri, R., Schneider, S. E., & Huchra, J. P. 2003, AJ, 125, 525
Jarrett, T. H., Chester, T., Cutri, R., et al. 2000, AJ, 119, 2498
Jeans, J. H. 1915, MNRAS, 76, 70
Kamphuis, J., & Briggs, F. 1992, A&A, 253, 335
Kauffmann, G., Colberg, J. M., Diaferio, A., & White, S. D. M. 1999, MNRAS, 303, 188
Kelz, A., Verheijen, M. A. W., Roth, M. M., et al. 2006, PASP, 118, 129
Kennicutt, R. C., Jr. 1998, ApJ, 498, 541
Kennicutt, R. C., Jr., Armus, L., Bendo, G., et al. 2003, PASP, 115, 928
Kennicutt, R. C., Jr., & Evans, N. J. 2012, ARA&A, 50, 531
Kewley, L. J., Dopita, M. A., Sutherland, R. S., Heisler, C. A., & Trevena, J. 2001, ApJ, 556, 121
Kormendy, J., & Illingworth, G. 1982, ApJ, 256, 460
Kormendy, J., & Kennicutt, R. C., Jr. 2004, ARA&A, 42, 603
Krajnović, D., Cappellari, M., de Zeeuw, P. T., & Copin, Y. 2006, MNRAS, 366, 787
Krumholz, M. R., McKee, C. F., & Tumlinson, J. 2009, ApJ, 699, 850
Law, D. R., Steidel, C. C., Erb, D. K., et al. 2007, ApJ, 669, 929
Lee, J. C., Gil de Paz, A., Tremonti, C., et al. 2009, ApJ, 706, 599
Lemoine-Busserolle, M., Bunker, A., Lamareille, F., & Kissler-Patig, M. 2010, MNRAS, 401, 1657
Leroy, A. K., Walter, F., Brinks, E., et al. 2008, AJ, 136, 2782
Macri, L. M., Stetson, P. B., Bothun, G. D., et al. 2001, ApJ, 559, 243
Massey, P., Strobel, K., Barnes, J. V., & Anderson, E. 1988, ApJ, 328, 315
Mathis, J. S. 2000, ApJ, 544, 347
McCall, M. L., Rybski, P. M., & Shields, G. A. 1985, ApJS, 57, 1
McKee, C. F., & Ostriker, E. C. 2007, ARA&A, 45, 565
Mould, J. R., Huchra, J. P., Freedman, W. L., et al. 2000, ApJ, 529, 786
Moustakas, J., & Kennicutt, R. C., Jr. 2006, ApJS, 164, 81
Moustakas, J., Kennicutt, R. C., Jr., Tremonti, C. A., et al. 2010, ApJS, 190, 233
Oke, J. B. 1990, AJ, 99, 1621
Osterbrock, D. E., & Ferland, G. J. (ed.) 2006, Astrophysics of Gaseous Nebulae and Active Galactic Nuclei (2nd. ed.; Sausalito, CA: Univ. Science Books)
Paturel, G., Petit, C., Garnier, R., & Prugniel, P. 2000, yCat, 414, 40475
Pei, Y. C. 1992, ApJ, 395, 130
Rizzi, L., Tully, R. B., Makarov, D., et al. 2007, ApJ, 661, 815
Rosales-Ortega, F. F., Díaz, A. I., Kennicutt, R. C., & Sánchez, S. F. 2011, MNRAS, 415, 2439
Rosales-Ortega, F. F., Kennicutt, R. C., Sánchez, S. F., et al. 2010, MNRAS, 405, 735
Sánchez, S. F. 2006, AN, 327, 850
Sanchez, S. F., Kennicutt, R. C., Gil de Paz, A., et al. 2012, A&A, 538, A8
Sánchez, S. F., Rosales-Ortega, F. F., Kennicutt, R. C., et al. 2011, MNRAS, 410, 313
Sánchez-Blázquez, P., Peletier, R. F., Jiménez-Vicente, J., et al. 2006, MNRAS, 371, 703
Sarzi, M., Falcón-Barroso, J., Davies, R. L., et al. 2006, MNRAS, 366, 1151
Schlegel, D. J., Finkbeiner, D. P., & Davis, M. 1998, ApJ, 500, 525
Somerville, R. S., & Primack, J. R. 1999, MNRAS, 310, 1087
Springob, C. M., Masters, K. L., Haynes, M. P., Giovanelli, R., & Marinoni, C. 2009, ApJS, 182, 474
Stromberg, G. 1922, PNAS, 8, 141
Thilker, D. A., Bianchi, L., Meurer, G., et al. 2007, ApJS, 173, 538
Thompson, T. A. 2009, in ASP Conf. Ser. 408, The Starburst-AGN Connection, ed. W. Wang, Z. Yang, Z. Luo, & Z. Chen (San Francisco, CA: ASP), 128
Toomre, A., & Toomre, J. 1972, ApJ, 178, 623
Tully, R. B. 1974, ApJS, 27, 415
Tully, R. B. 1988, Nearby Galaxies Catalog (Cambridge: Cambridge Univ. Press), 221
Tully, R. B., & Fisher, J. R. 1977, A&A, 54, 661
Tully, R. B., Rizzi, L., Shaya, E. J., et al. 2009, AJ, 138, 323
van de Voort, F., Schaye, J., Altay, G., & Theuns, T. 2012, MNRAS, 421, 2809
van der Kruit, P. C. 1988, A&A, 192, 117
van der Kruit, P. C., & Freeman, K. C. 2011, ARA&A, 49, 301
van Dokkum, P. G. 2001, PASP, 113, 1420
Verheijen, M. A. W. 2001, ApJ, 563, 694
Walter, F., Brinks, E., de Blok, W. J. G., et al. 2008, AJ, 136, 2563
Weinzirl, T., Jogee, S., Khochfar, S., Burkert, A., & Kormendy, J. 2009, ApJ, 696, 411
White, S. D. M., Tully, R. B., & Davis, M. 1988, ApJL, 333, L45
Wong, T., Blitz, L., & Bosma, A. 2004, ApJ, 605, 183
Wright, S. A., Larkin, J. E., Barczys, M., et al. 2007, ApJ, 658, 78
York, D. G., Adelman, J., Anderson, J. E., Jr., et al. 2000, AJ, 120, 1579